Insights into upper lithosphere detachment and exhumation through numerical modelling

[*]Dimitrios Papadomarkakis, Constantin D. Athanassas

Department of Geological Sciences, School of Mining and Metallurgical Engineering, National Technical University of Athens, 9 Iroon Polytechneiou Str., GR15780, Zografou Campus, Athens, Greece

Dear Editor,

I am here submitting a research paper entitled "Insights into upper lithosphere detachment and exhumation through numerical modeling" to be considered for publication in *EarthArxiv*. This article has not been submitted for peer review in any journal.
We hope it will be of interest to the readership of *EarthArxiv*.

On behalf of my co-authors,

Sincerely yours,

Dimitrios Papadomarkakis

Constantin D. Athanassas email address: athanassas@central.ntua.gr
Dimitrios Papadomarkakis email address: papadomarkakisdimitrios@gmail.com

Insights into upper lithosphere detachment and exhumation through numerical modelling

*Dimitrios Papadomarkakis, Constantin D. Athanassas

Department of Geological Sciences, School of Mining and Metallurgical Engineering, National Technical University of Athens, 9 Iroon Polytechneiou Str., GR15780, Zografou Campus, Athens, Greece

Abstract

The mechanisms underlying exhumation have been a topic of debate among researchers for many decades, prompting the development of numerous computational models aimed at elucidating the processes that initiate exhumation. However, a key gap in the literature lies in understanding how segments of the subducting lithospheric plate detach and subsequently exhumate after extended periods. Specifically, there has been limited investigation into whether material is stripped from the upper portion of the downgoing plate at relatively shallow depths, approximately 30 km, and, if so, whether these segments can eventually reach the Earth's surface. Furthermore, no existing model demonstrates that material can detach from the subducting plate as early as 15,000 years after the subduction is initiated. This study seeks to examine whether such a phenomenon occurs, using the subduction system of the Mediterranean Ridge as a case study. The process was simulated by extensively modifying an established thermomechanical visco-elasto-plastic code, named I2ELVIS, initially introduced by Gerya (2010). Lastly, macroscopic observations from the broader Hellenides region were employed to ascertain whether any such metamorphic rocks had indeed surfaced, thus confirming their exhumation. In conclusion, this research serves as a foundational investigation into a subject that warrants further exploration and detailed analysis in the future.

Keywords: 2-D geodynamic modelling, subduction zones, exhumation mechanisms, mantle rheology, detachment mechanisms.

*Corresponding author, E-mail address: papadomarkakisdimitrios@gmail.com

1. Introduction

Subduction zones are regions where ageing lithospheric material is recycled back into the mantle (Gerya et al., 2002). These zones, comprising a subducting lithospheric plate beneath an overlying plate, have been modelled extensively by numerous researchers using numerical methods (Neil and Houseman, 1999; Gerya et al., 2002; Gerya and Yuen, 2003a; Raimbourg et al., 2007; Warren et al., 2008a, 2008b; Beaumont et al., 2009; Li et al., 2012). One of the key geodynamic processes that has gathered significant attention in subduction settings is the exhumation of lithospheric rocks. The most commonly examined phenomenon of the latter is the kinetics and mechanisms of either ultra high-pressure metamorphic rocks or either high-pressure metamorphic rocks, both of which have been extensively researched (Platt, 1993; Chemenda et al., 1996; Gerya et al., 2002; Warren et al., 2008a, 2008b; Beaumont et al., 2009).

In general, the exhumation mechanisms and processes of (ultra)-high and high pressure metamorphic rocks have been widely debated over the past decades, with many researchers supporting that the formation of the gravitational instability, also known as the Rayleigh-Taylor instability, is the main driving force for the exhumation of deep buried material (Neil et al., 1999; Gerya and Yuen, 2003a). This instability is characterized by its diapiric formations, also known as ‘’plumes’’, that require millions of years to fully develop. When fully developed, it is believed that they completely detach from the subducting plate and enter the flowing mantle, where they are subjected to high pressure and temperature conditions that induce their metamorphism. These metamorphic rocks are than most likely exhumed.

On the other hand, the same process has been extensively modelled by researchers using lubrication theory (England and Holland, 1979; Cloos, 1982; Cloos and Shreve, 1988a, 1988b; Mancktelow, 1995; Raimbourg et al., 2007; Warren et al., 2008a, 2008b; Beaumont et al., 2009; Li, 2014), if it is considered that the subducting plate is governed by two competing flows, a down channel Couette flow and an up channel Poiseuille flow. In these models, the lithospheric slab is understood to exhibit two competing flows: one promoting the burial of material and the other facilitating its exhumation.

Another exhumation mechanism that has been suggested in the past 25 years, is a buoyancy driven exhumation, that originates from the density difference between the detached rock and the flowing mantle. Particularly, the latter mechanism is proposed to be the dominant one when the flowing mantle has a higher density value than that of the detached rock, thus creating an upwards buoyancy force that possibly exhumes the rock. This exhumation mechanism has been suggested and utilised by many researches over the years (Liou et al., 2004; Warren et al., 2008a, 2008b; Beaumont et al., 2009; Warren, 2013), in order to explain (ultra) high-pressure rock exhumations in the Alpine and Himalayan regions. Additionally, it has also been suggested that rock exhumation, which is governed by buoyancy, allows the detached rocks to reside in the (ultra) high pressure conditions for a very short time, less than 5 Myr (Rubatto and Hermann, 2001).

These studies have consistently shown that the exhumation process can take over 25 million years (Gerya and Yuen, 2003a; Li et al., 2012), with the detachment of exhumed material typically occurring in the lower parts of the asthenosphere at depths of 80-120 km

(Gerya and Yuen, 2003a), or even deeper, at 180-200 km (Warren et al., 2008a, 2008b). However, there have been no previous modelling attempts that have explored whether lithospheric material could detach from the subducting plate at much shallower depths, particularly in the upper parts of the lithosphere at depths as shallow as 30 km, and whether this detached material could eventually reach the surface. Additionally, it has not been investigated whether this detachment from the subducting plate could occur over a relatively short geological timescale, specifically in less than 20,000 years.

Despite this large existing gap in the available literature, previous macroscopic observations conducted by Thomson et al. (1998) in the island of Crete provided clear evidence that HP/LT exhumed metamorphic rocks had been detached from the downgoing plate from the shallow depths of around 30-35 km. These detached rocks from the subducting plate were subjected to high pressures and relatively low temperatures, thus causing the metamorphism of the granite rock into gneiss, which is mostly composed of quartz. Overall, such HP/LT exhumed metamorphic rock have been widely studied and observed in the Greek island of Crete (Fassoulas et al., 1994; Thomson et al., 1998; Chatzaras et al., 2006; Ring et al., 2010). Thus, although evidence from previous macroscopic geological observations suggests that lithospheric material can detach from the subducting plate at shallow depths of approximately 30 km, no numerical model has been developed to definitively confirm this phenomenon or to determine the time required for its occurrence.

To sum up the aim of the study was firstly to investigate whether at the shallow depths of the lithosphere, particularly close to 30 km, if the upper deformed part of the downgoing plate endures such increased strain values that the detachment of rock segments occurs and to observe if the detachment can take place within a relatively short timescale, as early as 15,000 years from the initiation of the subduction. In order to properly address the above-mentioned questions a computational model was developed for the subduction zone of the Mediterranean Ridge, located south of Crete. This was achieved using a two-dimensional thermomechanical visco-elasto-plastic code originally introduced by Gerya (2010), named I2ELVIS. Finally, macroscopic geological observations from the Hellenides were utilized in order to assess whether these shallow depth detached lithospheric rocks were exhumed.

2. 2-D Model Setup

2.1. Structure of the Model

In the original computational model created by Gerya (2010), three different layers were present. First, the "weak medium" layer represented the flowing mantle, which was adapted in later versions of the code. Second, the "block" layer was modified to resemble the thin upper layer of the subducting lithospheric slab, which had undergone significant tectonic deformation. The existence of this thin upper rock layer has been proposed by various researchers (Capitanio et al., 2007; Royden and Papanikolaou, 2011; Goes et al., 2011). Finally, the "weak inclusion" layer was removed entirely, as it served no purpose in the current geodynamic context. A new layer, the "lower weak medium," was added by the authors. This layer represented the lower part of the subducting lithospheric plate, characterised by much stiffer properties compared to the thin upper layer. The latter acted as the interface between the flowing mantle and the rest of the slab.

The initial model size of the computational setting was 1,000 km in both the horizontal and vertical axes. Additionally, 51 nodes were placed along both axes, and 40,000 markers were randomly distributed throughout the model (Gerya, 2010). To improve the visualisation of the results, the horizontal length was reduced by 800 km, resulting in a new length of 200 km, while the vertical length was shortened to 80 km. Despite these changes, the number of nodes and markers remained the same, maintaining 51 nodes in both directions and 40,000 randomly distributed markers.

Overall, the computational model's structure consisted of a flowing mantle and a subducting lithospheric plate divided into two uneven layers. The upper thin layer was more heavily deformed due to its constant interaction with the mantle, while the lower, thicker layer, which made up most of the plate, exhibited less deformation. Figure 1 provides a visual representation of the computational model. The subducting system was modelled after the Hellenic subduction zone, commonly referred to as the Mediterranean Ridge, located south of Crete. Geophysical investigations have confirmed that the Moho zone's depth in this region begins at approximately 25–30 km below the surface (Makris, 2010; Makris et al., 2013). Consequently, it was assumed that the subduction process initiates at this same depth, aligning with the Moho zone's starting depth. This approximation was consistent with the resemblance between the map of the Moho zone surface, as derived from geophysical data (Makris et al., 2013), and the typical topography of a subducting and overriding plate.

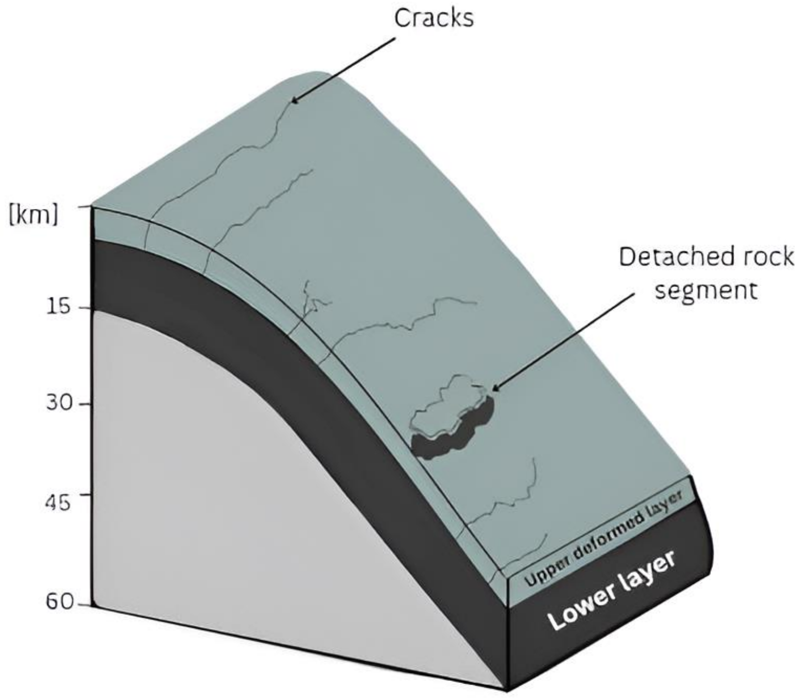

Figure 1: In this figure, the subducting plate is depicted, highlighting its two distinct, uneven layers. Additionally, select outcomes from the computational simulation are illustrated, particularly the onset of cracking in the upper deformed layer of the slab and the eventual detachment of a rock segment. These results will be comprehensively presented and analysed in the relevant sections of this study.

In the computational model, only a section of the subducting plate is visualised. Additionally, a justified approximation was made by the authors to simplify the visualisation of the results at each timestep. Specifically, no subduction rate was assigned to the slab, effectively treating it as a stagnant plate. The reasoning behind this approximation lies in the relatively short simulation time of around 15,000 years, which is considered brief in comparison to the much longer timescales over which geodynamic processes typically occur. As such, it was assumed that the slab did not move significantly enough during this period to substantially influence the results. Therefore, the subduction rate was entirely neglected in the current simulation.

2.2. Material Properties and Boundary Conditions

The material properties of each of the aforementioned layers were significantly modified to meet the objectives and requirements of this research. Specifically, Table 1 presents all the values utilised for the material properties. Most of these values have been extensively studied and recommended by previous researchers (Capitanio et al., 2007; Makris, 2010; Royden and Papanikolaou, 2011; Makris et al., 2013).

Table 1 In this table the values of all the material properties are presented.

Parameters	Flowing Mantle	Stagnated Slab	Thin Rock Layer
Viscosity (Pa s)	$3x10^{20}$	10^{24}	10^{22}
Density (kg/m^3)	3300	2800	2800
Thermal Conductivity (W/mK)	2.55	2.4	2.55
Thermal Expansion (1/K)	$5.8x10^{-8}$	10^{-7}	$5.8x10^{-8}$
Radioactive Heating (W/m^3)	10^{-6}	10^{-7}	10^{-6}
Heat Capacity (J/kg)	750	650	750
Shear Modulus (Pa)	10^{10}	$15x10^{9}$	$22.8x10^{9}$
Cohesion (Pa)	$28.4x10^{6}$	$11.5x10^{6}$	10^{11}
Friction Coefficient	0.3	0.6	0.7
Temperature (K)	520	400	400

Firstly, the viscosity was initially set at 10^{23} Pa·s for the subducting slab and at 10^{17} Pa·s for the flowing mantle. The value for the lower part of the subducting slab was increased, as this section was expected to be stiff rather than viscous. Additionally, the original density values were 4000 kg/m^3 for the stagnated slab and 1 kg/m^3 for the flowing mantle. These values were completely revised since they represented materials not typically present in geodynamic processes. The rationale for the chosen density values can be explained by the chemical composition of the flowing mantle and the subducting plate. Particularly, the flowing mantle was considered to be primarily composed of peridotite, thus justifying the density value of 3,300 kg/m^3. This density value was also used by Royden and Papanikolaou (2011) in their modelling of the segmentation of the Hellenic arc and later verified by geophysical investigations (Makris et al., 2013). As for the subducting slab, both the lower, thicker layer and the upper, thinner layer were assumed to be predominantly composed of granite, giving them a density value of approximately 2,800 kg/m^3 (Makris, 2010; Royden and Papanikolaou, 2011; Makris et al., 2013).

Moreover, several thermomechanical parameters were altered, including thermal conductivity, thermal expansion, radioactive heating, and heat capacity. The shear modulus values were also adjusted, as the original code assigned a uniform value of 10^{10} Pa for both the mantle and the slab. Consequently, the cohesion and friction coefficient values were extensively modified, with the cohesion of the lower part of the plate being significantly increased to ensure its impermeability against the flowing mantle. Finally, the original mantle and slab temperatures were set at 1000 K and 1300 K, respectively. Both were reduced due to the relatively shallow depth of approximately 30 km at which the process occurs.

In general, the temperatures at the boundaries of the computational model, including the upper, lower, right, and left boundaries, were held constant. Specifically, the upper and right boundaries were set to a constant temperature of 520 K, consistent with that of the mantle, while the lower and left boundaries were set to 400 K, mirroring the temperature of the slab. These boundaries were characterised as insulating, thus implying that no heat flux occurred through the boundary, meaning no temperature gradient existed across it.

In addition to the no heat flux condition, a lateral symmetry condition is applied, which is widely used in both 2D and 3D Cartesian geodynamic models (Gerya, 2010). Furthermore, to simplify the fluid flow analysis, a free-slip boundary condition was employed, ensuring that no frictional forces act parallel to the boundary surface.

2.3. Driving Subduction and Detachment Forces

The primary forces exerted on the thin upper layer of the plate include the buoyancy force (F_b), which acts in the direction of the surface (Capitanio et al., 2007; Goes et al., 2011). This buoyancy force arises because the slab is essentially submerged in the flowing mantle, a viscous fluid, and as a natural response, the fluid exerts an upward force to make the thin layer float. Additionally, the weight force (F_w) acts in opposition to the buoyancy force. Furthermore, a lithostatic pressure force (F_P) is also applied, with the same downward direction as the weight force (Turcotte and Schubert, 1982). Lastly, there is a viscous force (F_V) due to the flowing mantle, which acts parallel to the slab's surface and upwards, resisting the plate's subduction (Royden and Papanikolaou, 2011). All these forces are depicted in Figure 2.

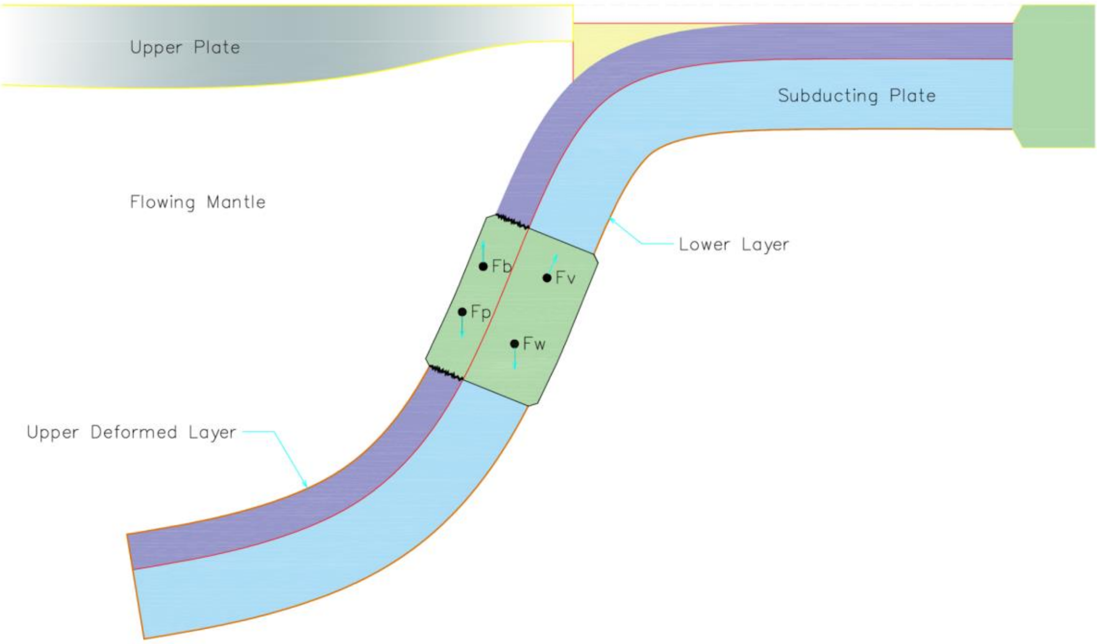

Figure 2: This figure depicts the forces exerted on a rock segment situated within the upper deformed layer of the subducting plate, highlighting those that promote the burial of the segment (weight and pressure forces) and those that drive it upwards (buoyancy and viscous forces).

In summary, the driving forces behind subduction are the weight force and the pressure force, which together promote the downward motion of the plate. Conversely, the buoyancy force and the viscous force resist the slab's subduction. The balance between these driving and resisting forces governs the subduction process (Forsyth and Uyeda, 1975; Vlaar and Wortel, 1976; Chapple and Tullis, 1977; Davies, 1988; Capitanio et al., 2007).

2.4. Potential Development of the Rayleigh–Taylor Gravitational Instability

An important phenomenon that warrants discussion is the Rayleigh-Taylor gravitational instability. This instability occurs when a heavier fluid (in this case, the mantle) overlies a lighter fluid (the lithospheric slab), leading to a gravitational imbalance. The interface between the two fluids becomes distorted, causing fluid motions, and ultimately, the heavier mantle is penetrated by the lighter, underlying slab. The resulting effect is the formation of characteristic diapiric structure, often described as a "mushroom-like" shape, as the lighter fluid rises through the heavier fluid (Turcotte and Schubert, 1982). The Rayleigh-Taylor instability has been extensively modelled by various researchers (Turcotte and Schubert, 1982; Neil et al., 1999; Gerya and Yuen, 2003a; Kaus and Becker, 2006; Ghosh et al., 2020) because it is believed that the resulting "cold" plumes produced by this instability have a strong likelihood of being exhumed. Despite the fact that the appropriate conditions for the initiation of the Rayleigh-Taylor gravitational instability were present at this computational setting, the phenomenon was completely dismissed from the simulation. The reason for its exclusion is grounded in prior studies (Neil et al., 1999; Gerya and Yuen, 2003a), which demonstrate that the full development of the instability, including the diapiric formation that may eventually be exhumed, typically requires around 25 million years (Gerya and Yuen, 2003a) to form. Given that the simulations conducted in the present study spanned only 15,000 years, a brief period in geological time, there was insufficient time for the Rayleigh-Taylor instability to develop to a stage where it would affect the outcomes of the model. As such, this phenomenon was neglected to simplify the overall computational framework.

3. Analytical Rheological Modelling

3.1. Down-Channel Couette Flow

Firstly, within the ''flowing'' subducting channel, exists a down-channel Couette flow, commonly referred to as the subducting flow, which promotes the burial of the upper deformed material (Raimbourg et al., 2007; Warren et al., 2008a, 2008b; Beaumont et al., 2009; Li, 2014). This downward Couette flow is given by the following equation (Raimbourg et al., 2007; Warren et al., 2008a, 2008b; Beaumont et al., 2009; Li, 2014):

$$u_{couette} = U(1 - \frac{y}{h})\ (9),$$

where, $u_{couette}$: is the downgoing Couette flow velocity, U: denotes the subduction velocity of the underlying lithosphere, x: is measured in the down-dip direction, y: is the position in the channel measured normal to the base and h: is the channel (lithosphere) thickness.

3.2. Up-Channel Poiseuille Flow

Secondly, the competing flow within the subducting channel is an up-channel Poiseuille flow, commonly referred to as the exhumation flow, which promotes the upward movement of the deformed upper section of the subducting plate (Raimbourg et al., 2007; Warren et al., 2008a, 2008b; Beaumont et al., 2009; Li, 2014). This up-channel flow is primarily driven by the buoyancy of the low-density subducted material, in contrast to the denser mantle, and by the viscous resistance of the mantle, which counteracts the downward motion of the plate (Raimbourg et al., 2007; Warren et al., 2008a, 2008b; Beaumont et al., 2009; Li, 2014). The Poiseuille flow can be described by the following equation (Raimbourg et al., 2007; Warren et al., 2008a, 2008b; Beaumont et al., 2009; Li, 2014):

$$u_{Poiseuille} = (\frac{1}{2n})(\frac{\vartheta P}{\vartheta x})(yh - y^2)\ (10),$$

where, $u_{Poiseuille}$: is the up-channel Poiseuille flow velocity, n: is the uniform viscosity and $\frac{\vartheta P}{\vartheta x}$: denotes the effective down-channel pressure gradient.

3.3. Lubrication Theory

These two competing flows, which are present within the viscous channel of the subducting plate, have been extensively studied by numerous researchers in the past through the application of lubrication theory (England and Holland, 1979; Cloos, 1982; Cloos and Shreve, 1988a, 1988b; Mancktelow, 1995; Raimbourg et al., 2007; Warren et al., 2008a, 2008b; Beaumont et al., 2009; Li, 2014). Under the assumptions of lubrication theory (Pozrikidis, 2001), which postulates that the overlying lithospheric plate remains stationary, the velocity of flow within the channel is expressed by the following equation:

$$u(x,y) = -(\frac{1}{2n})(\frac{\vartheta P}{\vartheta x})(yh - y^2) + U(1 - \frac{y}{h})\ (11).$$

Additionally, when the non-dimensional variables: $u' = u/U, h' = h/H, y' = y/h\ and\ x' = x/h$ are used, Eq. (11) is reduced to:

$$u' = -Eh'^2 \frac{(y' - y'^2)}{2 + (1 - y')}\ (12),$$

where,

$$E = (H^2 \times \frac{\vartheta P}{\vartheta x})/(n_{eff}U)\ (13),$$

$$H = (\frac{2n_{eff}U}{\vartheta P/\vartheta x})^{1/2}\ (14),$$

where, n_{eff}: represents the effective viscosity and the parameter H: is the characteristic channel (slab) thickness for E=1, the balance point between the downward and returning flows. All of the parameters along with the flow directions can be seen in Figure 3.

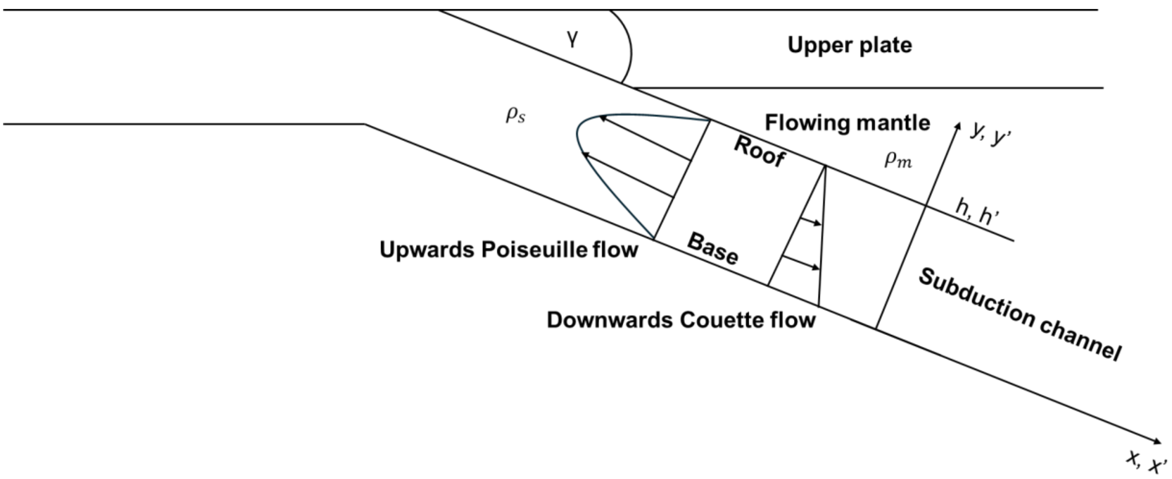

Figure 3: This figure illustrates the two competing flows, particularly, the downgoing Couette flow and the up-channel Poiseuille, along with other key parameters.

However, the key parameter in Eq. (12) is the exhumation number (E) (Warren et al., 2008a, 2008b; Beaumont et al., 2009; Li, 2014), which corresponds to the α parameter as described by Raimbourg et al. (2007). This parameter fundamentally quantifies the competition between the up-channel Poiseuille flow, and the down-channel Couette flow.

In cases where the channel walls are deformable, as in the present model, and there is no tectonic overpressure or underpressure, the pressure gradient depends on the density difference between the subducted material (granite) within the slab (channel) and the surrounding mantle (peridotite) and it is thus given by the following equation (Warren et al., 2008a, 2008b; Beaumont et al., 2009; Li, 2014):

$$\frac{\vartheta P}{\vartheta x} = (\rho_m - \rho_s) g sin(\gamma) \ (15),$$

where, $\rho_m \ and \ \rho_s$: are the density of the mantle and the lithospheric slab respectively and γ: represents the dip of the subduction channel.

Overall, there are three distinct scenarios that can arise depending on the exhumation number (E). The first scenario, occurs when the density of the subducting material (ρ_s) exceeds that of the surrounding mantle (ρ_m), thus $\rho_s \succ \rho_m$. In this case, the pressure gradient, as defined by Eq. (15), decreases along the channel, resulting in both $\frac{\vartheta P}{\vartheta x}$ and E being negative. As a consequence, the down-channel Couette flow dominates, leading to a low likelihood of exhumation.

The second scenario, occurs when the density of the subducting material equals the density of the surrounding mantle, thus $\rho_s = \rho_m$. In this instance, the pressure gradient and exhumation number equal zero, or more conveniently, E~1. This represents the balance point between the downward subducting flow and the upward return flow, leaving the slab stagnant.

Finally, the third scenario takes place when the density of the subducting material is less than that of the surrounding mantle, thus $\rho_s \preccurlyeq \rho_m$, which is also the occurring scenario. Here, the pressure gradient increases along the channel, resulting in both $\frac{\vartheta P}{\vartheta x}$ and E being positive. Buoyancy drives the upward flow in the channel, making the Poiseuille flow dominant (Raimbourg et al., 2007; Warren et al., 2008a, 2008b; Beaumont et al., 2009; Li, 2014) and significantly increasing the likelihood of exhumation. In this case, the greater the positive value of E, the higher the exhumation velocity.

However, it is important to note that buoyancy alone is a necessary but not sufficient condition for exhumation to occur (Raimbourg et al., 2007; Warren et al., 2008a, 2008b; Beaumont et al., 2009; Li, 2014). Other controlling factors, such as a decrease in effective viscosity (n_{eff}) play a critical role in driving E beyond the exhumation threshold. Generally, the exhumation number (E) should be viewed as a measure of the local exhumation potential. Even when the local threshold value is exceeded (E>1), efficient exhumation may still be hindered by constrictions (low h) or high effective viscosities (n_{eff}) further up the channel (Raimbourg et al., 2007; Warren et al., 2008a, 2008b; Beaumont et al., 2009; Li, 2014).

To sum up, although it is not certain that exhumation will occur, it can be clearly observed that buoyancy is the driving force of the whole process thus further increasing the odds of detachment.

4. Numerical Modelling

4.1. Governing equations

Firstly, the x,y-Stokes equations for slow, viscous, incompressible flow in a uniform gravity field are expressed by the following formulas:

$$n(\frac{\vartheta^2 u_x}{\vartheta x^2} + \frac{\vartheta^2 u_x}{\vartheta y^2}) - \frac{\vartheta P}{\vartheta x} = \rho g_x \ (1)$$

$$n(\frac{\vartheta^2 u_y}{\vartheta x^2} + \frac{\vartheta^2 u_y}{\vartheta y^2}) - \frac{\vartheta P}{\vartheta y} = \rho g_y \ (2)$$

where, Eq. (1) represents the x-Stokes equation and Eq. (2) the y-Stokes equation respectively. Additionally, x and y denotes, respectively, the horizontal and vertical coordinates, the coefficient n: represents the effective viscosity (in Pa s), that depends on pressure, temperature and the velocity, P: stands for the pressure (in Pa), ρ: is the density (in kg/m^3), g_x and g_y: denote components of the vector of acceleration within the gravity field (in m/s^2) for the x–y 2D coordinate system and finally, u_x and u_y: represent the velocity components (m/s) in the x and y direction respectively. For simplification purposes in the computational calculations, the values of ρg_x and ρg_y were neglected as they remained constant throughout the simulation and did not significantly influence the overall results. This allowed for a reduction in computational complexity without affecting the accuracy of the final outcomes.

Furthermore, another important equation is that of mass conservation, which is primarily described by the continuity equation. It is also worth noting that the density (ρ) was assumed to be constant in all terms, an approximation commonly used in numerical geodynamic modelling, known as the Boussinesq approximation (Moresi and Solomatov, 1995; Trompert and Hansen, 1996; Albers, 2000; Gerya and Yuen, 2003b; Gerya, 2010). The continuity equation can be expressed in the following form, assuming incompressible flow:

$$\frac{\vartheta u_x}{\vartheta x} + \frac{\vartheta u_y}{\vartheta y} = 0 \ (3)$$

Finally, another fundamental equation used extensively during the computational steps was the two-dimensional temperature equation. This equation is expressed using the Lagrangian form of the heat conservation equation, which accounts for radioactive, adiabatic and shear heating production:

$$\rho \times C_p \times \frac{DT}{Dt} = -\frac{\vartheta q_x}{\vartheta x} - \frac{\vartheta q_y}{\vartheta y} + H_r + \ H_\alpha + H_s \ \ (4),$$

$$q_x = -k \times \frac{\vartheta T}{\vartheta x} \ (5),$$

$$q_y = -k \times \frac{\vartheta T}{\vartheta y} \ (6),$$

$$H_r = const,$$

$$H_a = T\alpha[u_x(\frac{\vartheta \mathrm{P}}{\vartheta \mathrm{x}}) + u_y(\frac{\vartheta \mathrm{P}}{\vartheta \mathrm{y}})] = T\alpha\rho(u_x g_x + u_y g_y)\ (7),$$

$$H_s = n(2\frac{\vartheta^2 u_x}{\vartheta x^2} + \frac{\vartheta^2 u_y}{\vartheta y^2} + [\frac{\vartheta u_x}{\vartheta y} + \frac{\vartheta u_y}{\vartheta x}]^2)\ (8),$$

where, C_P: is the isobaric heat capacity (in J/kgK), q_x and q_y: are horizontal and vertical heat fluxes (in W/m^2), k: is the variable thermal conductivity coefficient (in W/mK) and H_r, H_α, H_s: denote, respectively, radioactive, adiabatic and shear heating production (in W/m^3). It is also important to mention that for the sake of simplicity in the calculation of H_α, slight deviations in the dynamic pressure gradients $\frac{\vartheta \mathrm{P}}{\vartheta \mathrm{x}}$ and $\frac{\vartheta \mathrm{P}}{\vartheta \mathrm{y}}$ from the values ρg_x and ρg_y were neglected.

4.2. Characteristics Based Marker-In-Cell Method with Conservative Finite Differences Schemes

Overall, Eqs. (1)-(4) represent the primary equations employed to establish the computational model of the I2ELVIS code that was utilised. Additionally, these equations were solved at every timestep to ensure the accurate representation of the system's behaviour. The structure of the computational code can be broken down into nine steps, which involve the solution of the momentum, continuity and temperature equation, Eq. (1)-(4), by using finite-differences and the characteristic based marker-in-cell technique. These nine steps are not presented in this paper, since they are out of its primary scope, however they are introduced and consequently analysed and explained extensively in previous studies by Gerya and Yuen (2003b) and Gerya (2010).

4.3. Simulation Parameters

The simulation was executed twice to account for two different thicknesses of the upper deformed layer of the subducting slab. In the first simulation (experiment 1), the upper layer thickness was set at 5 km. Each simulation spanned 150 timesteps, representing a period of 15,000 years. During each timestep, three critical parameters were calculated and visualised on the computational map: viscosity (n), the second stress invariant (σ_{II}) and the second strain rate invariant ($\underline{\varepsilon_{II}}$). In the second simulation (experiment 2), the thickness of the upper deformed layer was increased to 10 km. Similar to the first simulation, during each timestep, the three key parameters, viscosity (n), second stress invariant (σ_{II}) and second strain rate invariant ($\underline{\varepsilon_{II}}$), were calculated and visualised on the computational map.

5. Model Results

5.1. Second Strain Rate Invariant

First and foremost in the following Figures, the visualisation of the second strain rate invariant is showcased for the whole model, as well as the distribution of the second strain invariant values, for various time steps of the simulation, across the 49 vertical available nodes that were located inside the upper thin part of the lithospheric slab, respectively. In the three-part Figure 4 the second strain rate invariant values for the whole computational model are presented, the thickness of the upper deformed part of the plate was set at 5 km:

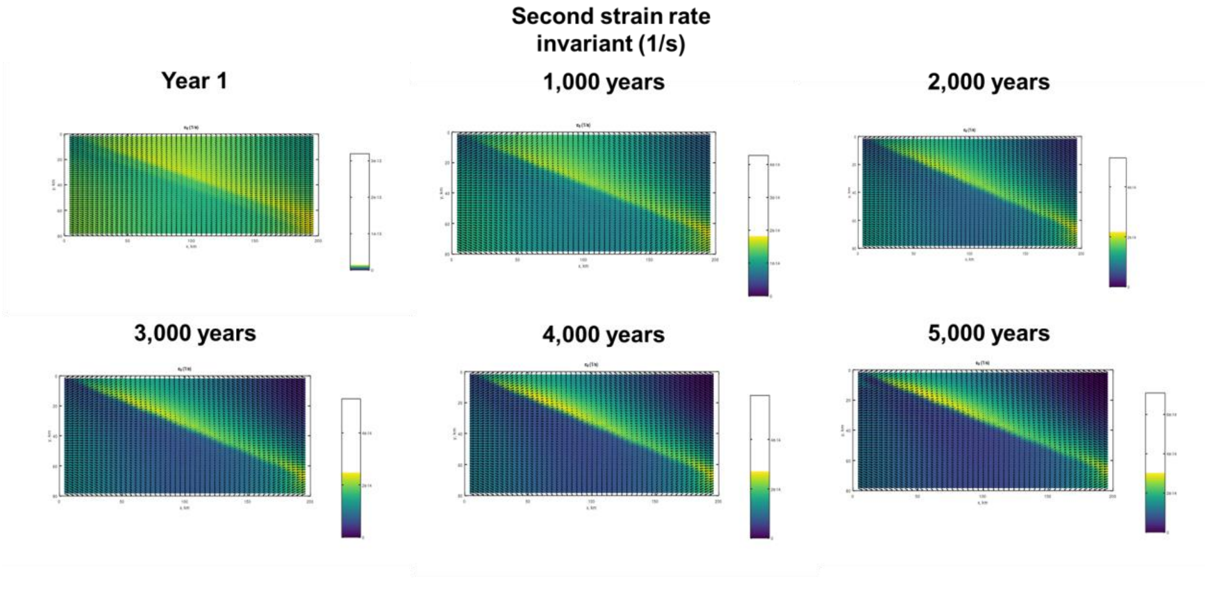

Part I

Figure 4: In part I of this figure the second strain rate invariant values are showcased for the computational model, when the thickness of the upper deformed layer was set at 5 km, particularly for the first year of the simulation, after 1,000 years, 2,000 years, 3,000, 4,000 and 5,000 years respectively.

In general, it can be seen that for the first 5,000 years of the simulation, a relatively high value of strain rate was present throughout the whole surface of the lithospheric slab and particularly in its upper left side, which is likely caused by the constant viscous flowing mantle.

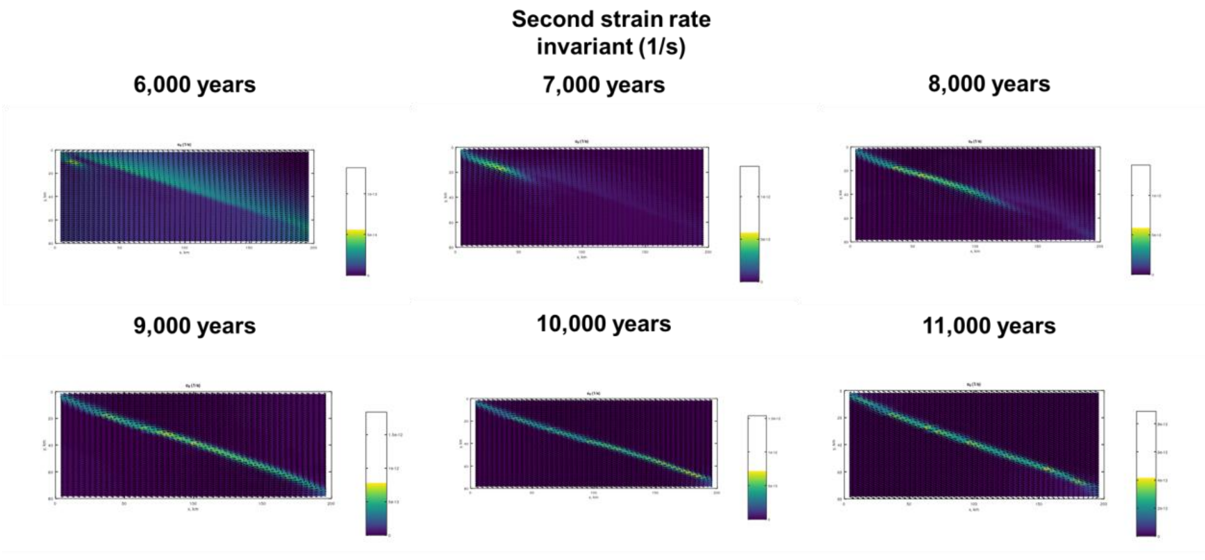

Part II

Figure 4: In part II of this figure the second strain rate invariant values are showcased for the computational model, when the thickness of the upper deformed layer was set at 5 km, particularly for the first year of the simulation, after 6,000 years from the initiation of the simulation, after 7,000 years, 8,000 years, 9,000, 10,000 and 11,000 years respectively.

After just 6,000 years from the start of the simulation, significant deformation is observed in the upper left section of the slab, where high strain rates persisted for nearly 5,000 years. This prolonged strain on the upper layer induced substantial deformation, potentially initiating cracks and possibly detaching sections of the material. Such damage and particularly the emergence of cracks may have allowed the infiltration of the viscous, flowing mantle into the upper deformed layer. Consequently, over the next 3,000 years, these cracks and the potential mantle intrusion propagated throughout the entire upper layer of the plate, establishing sustained high strain rates across its length.

In the final 4,000 years of the simulation (11,000-15,000 years), distinct patterns in strain rate values emerge within the heavily deformed upper layer, fluctuating between high and low values.

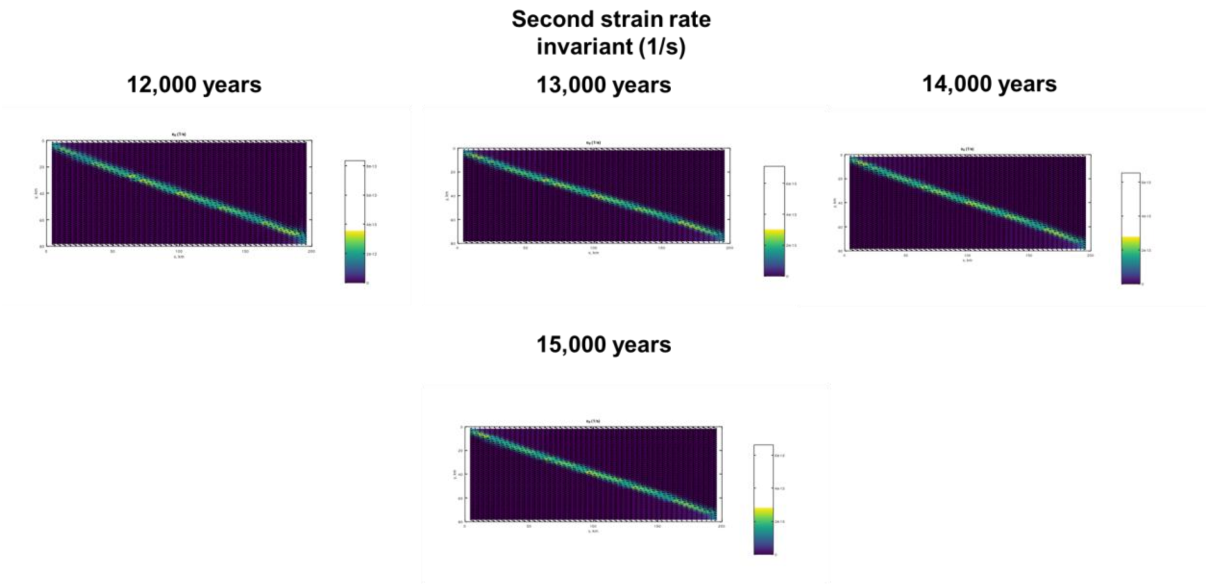

Part III

Figure 4: In part III of this figure the second strain rate invariant values are showcased for the computational model, when the thickness of the upper deformed layer was set at 5 km, particularly for the first year of the simulation, after 12,000 years from the initiation of the simulation, after 13,000 years, 14,000 and 15,000 years respectively.

Moreover, in the three-part Figure 5 the second strain rate invariant values for the whole computational model are presented, when the thickness of the upper deformed part of the plate was set at 10 km:

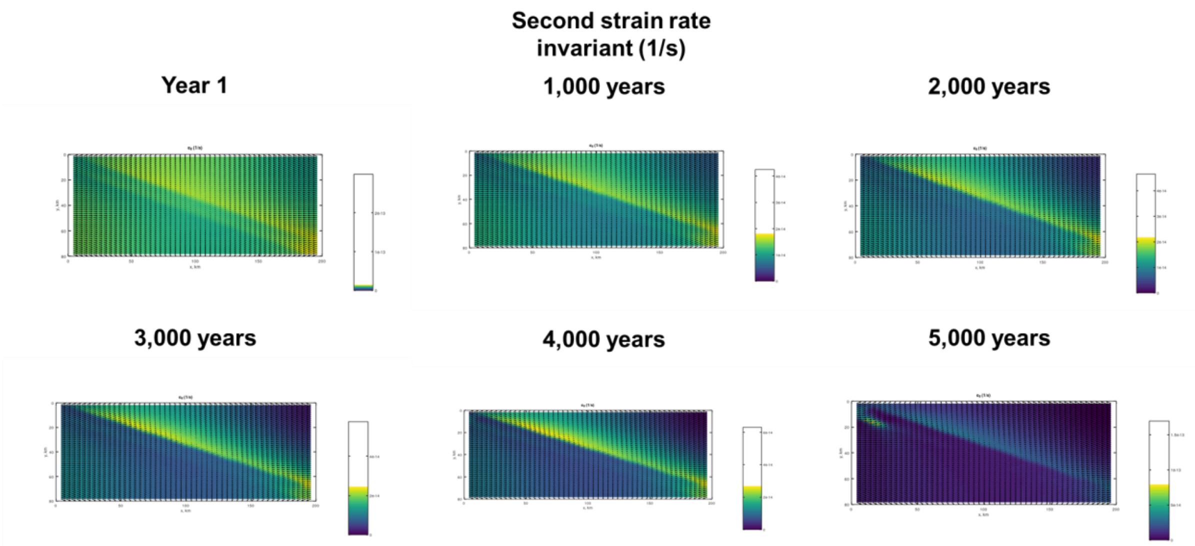

Part I

Figure 5: In part I of this figure the second strain rate invariant values are showcased for the computational model, when the thickness of the upper deformed layer was set at 10 km, particularly for the first year of the simulation, after 1,000 years, 2,000 years, 3,000, 4,000 and 5,000 years respectively.

As with the case of the 5 km thickness, the same high values of strain rate can be observed throughout the whole surface of the upper layer of the plate, again with the left side showcasing the larger values. The main difference with the 5 km model is that in the 10 km one the upper deformed layer displayed major deformation from the high strain rate values, and thus crack initiation, and consequently possible material detachment and entrance of the viscous flowing mantle, after only 5,000 years, almost 1,000 years earlier than the 5 km model.

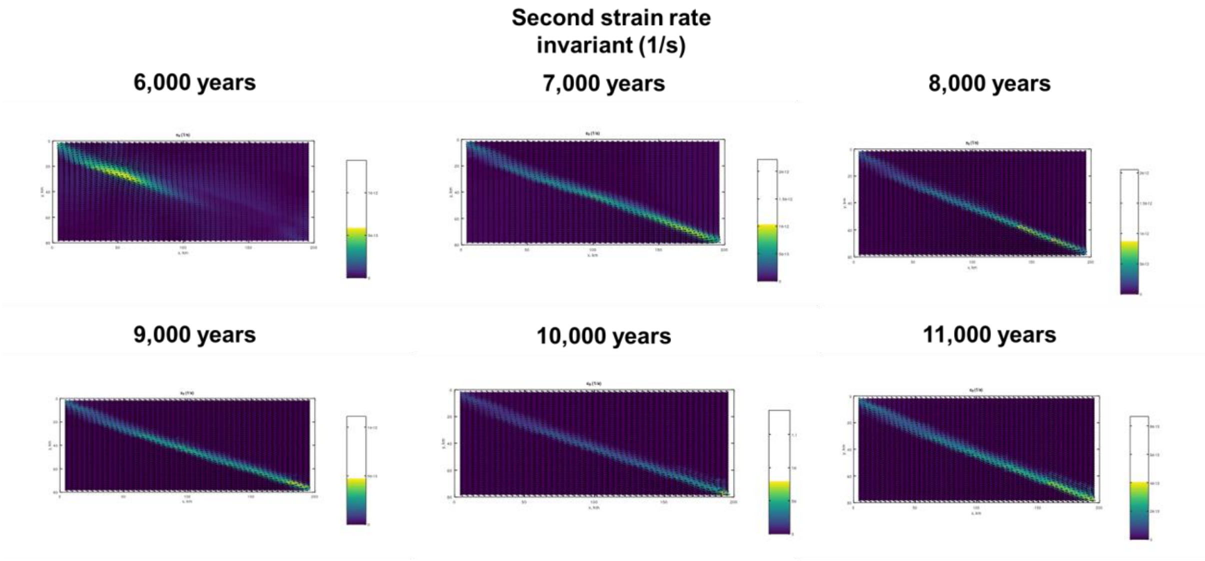

Part II

Figure 5: In part II of this figure the second strain rate invariant values are showcased for the computational model, when the thickness of the upper deformed layer was set at 10 km, particularly after 6,000 years from the initiation of the simulation, after 7,000 years, 8,000 years, 9,000, 10,000 and 11,000 years respectively.

Consequently, similar to the 5 km model, the cracks and potential infiltration of the flowing mantle extended throughout the entire upper layer of the plate. However, in the 10 km model, this process occurred over a much shorter time span, specifically within 2,000 years. From this point onward, significant strain rate values emerged along the length of this layer. Finally, consistent with the findings of the 5 km model, distinct patterns in strain rate values appear in the last 4,000 years of the simulation (11,000-15,000 years), fluctuating between high and low values within the heavily deformed upper layer.

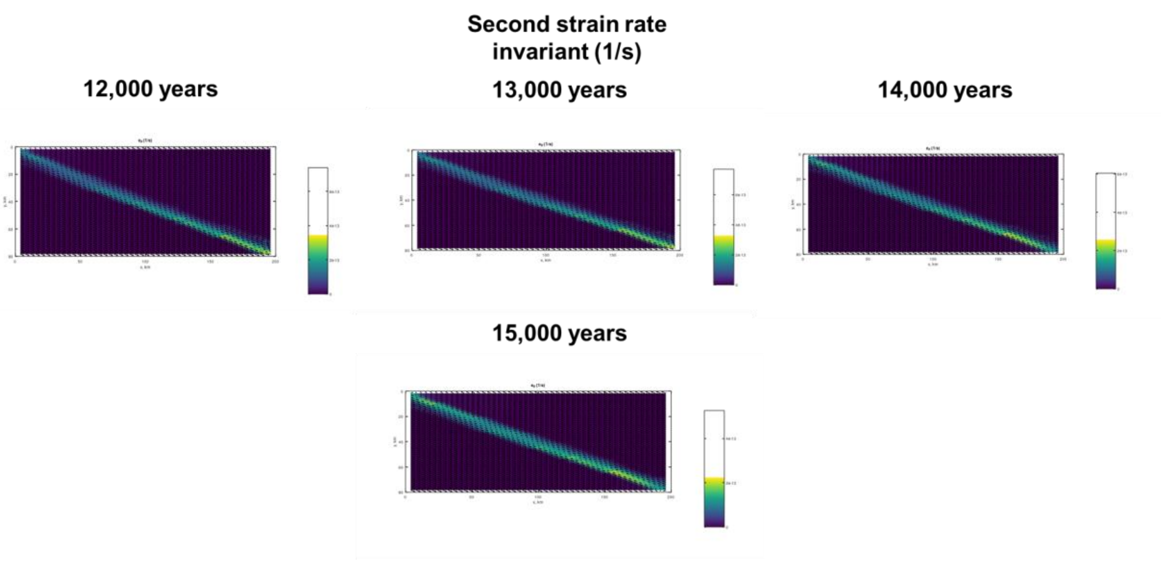

Part III

Figure 5: In part III of this figure the second strain rate invariant values are showcased for the computational model, when the thickness of the upper deformed layer was set at 10 km, particularly after 12,000 years from the initiation of the simulation, after 13,000 years, 14,000 and 15,000 years respectively.

Figure 6 illustrates the values of the second strain invariant for the upper layer of the plate with the thickness set at 5 km, evaluated at various significant time steps of the simulation. These values are analyzed across the 49 vertical nodes distributed throughout the entire length of the upper deformed layer of the slab. Specifically, the selected time intervals correspond to key moments of interest, namely the first year, the 1,000th year, and the 6,000th through 11,000th years in 1,000-year increments, as well as the 15,000th year.

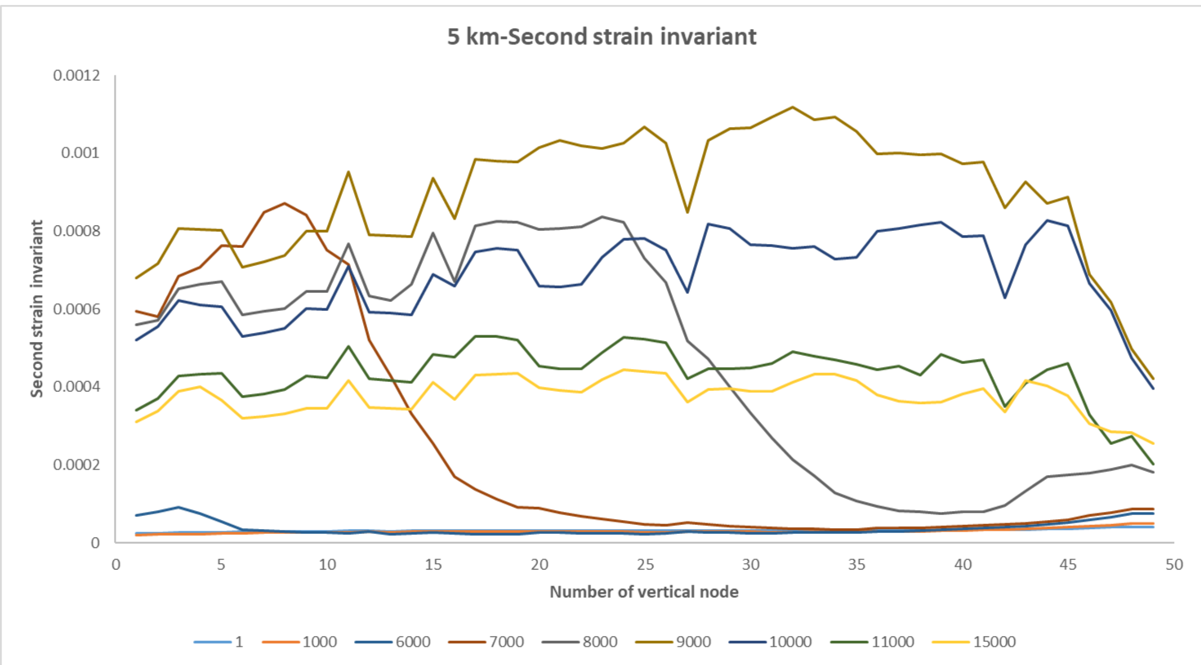

Figure 6: In this figure the second strain invariant values are presented, when the thickness of the upper layer of the plate was set at 5 km, for various important time moments of the simulation, in relation to the 49 vertical nodes that are located inside the upper deformed part of the lithospheric slab.

As previously observed in Fig. 4 (Part I), the strain values within the upper layer of the slab remain relatively low during the first 5,000 years, as significant strain is exerted primarily on the surface of the plate by the underlying mantle flow. However, by the 6,000th year, a slight increase in these low values becomes evident, attributed to the initiation of cracks in the left section of the slab, resulting in a minor spike in strain values. Subsequently, during the 7,000th and 8,000th years, the strain values increase significantly, affecting larger portions of the slab as the cracks propagate across most of the upper layer's length.

In the 9,000th year, the strain values reach their peak for the entire simulation, likely due to the cracks permeating the entire slab, suggesting material removal throughout the upper layer and mantle infiltration through the cracks. During the final 5,000 years of the simulation (10,000–15,000 years), the strain values exhibit a consistent pattern of local maxima and minima with minor variations, broadly aligning with the trends observed in Fig. 4 (Part III).

Accordingly, Figure 7 presents the second strain invariant values for an upper layer thickness of 10 km, evaluated at various significant time steps of the simulation. The selected time steps correspond to moments of particular interest, specifically the first year, the 1,000th year, and the 5,000th through 8,000th years in 1,000-year increments, followed by the 11,000th and 15,000th years.

Consistent with the observations derived from Fig. 5 (Part I), during the initial 4,000 years of the simulation, the strain values within the upper layer of the plate remain relatively low, as significant strain is exerted predominantly on the slab's surface by the mantle. By the 5,000th year, minor increases in strain are evident in the left portion of the slab, likely resulting from the initiation of cracks and the onset of lithospheric material detachment. By the 6,000th year, strain values have significantly increased across nearly half of the upper layer, driven by the propagation of cracks and the advancing infiltration of mantle material.

In the 7,000th year, the entire upper layer exhibits severe deformation, with strain values reaching their highest levels observed in the simulation. This deformation may indicate the detachment of material from the slab. During the remaining simulation period (8,000–15,000 years), the strain values display a generally consistent pattern of local maxima and minima, with only minor variations.

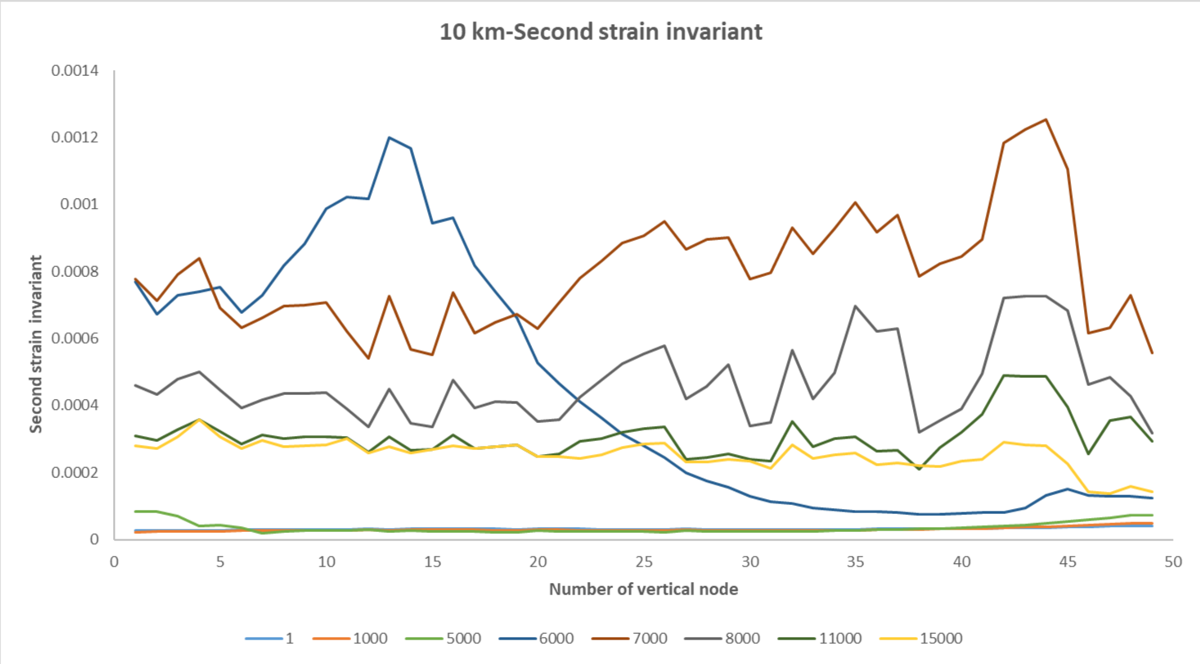

Figure 7: In this figure the second strain invariant values are presented, when the thickness of the upper layer of the plate was set at 10 km, for various important time moments of the simulation, in relation to the 49 vertical nodes that are located inside the upper deformed part of the lithospheric slab.

5.2. Second Stress Invariant

In the following three-part Figure 6 the second stress invariant values for the whole computational model are presented, when the thickness of the upper deformed part of the plate was set at 5 km:

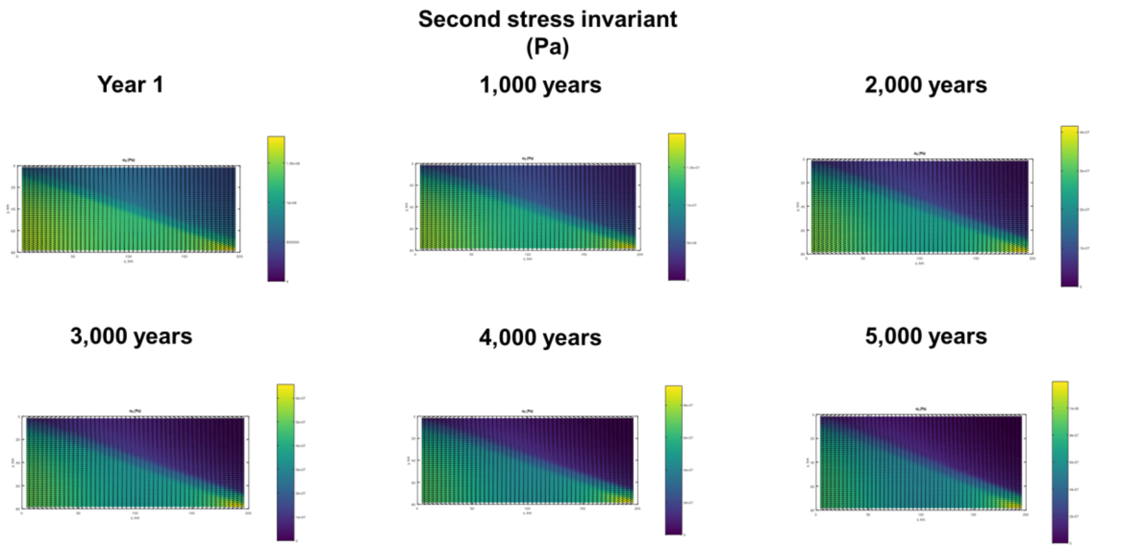

Part I

Figure 8: In part I of this figure the second stress invariant values are showcased for the computational model, when the thickness of the upper deformed layer was set at 5 km, particularly for the first year of the simulation, after 1,000 years, 2,000 years, 3,000, 4,000 and 5,000 years respectively.

In contrast, with the strain rate values, the stress values in the surface of the upper part of the plate are generally low, with the highest stress values mostly located in the lower, more stiffer parts of the plate. Additionally, it can be seen that the stress values have a slight increasing tendency with the passage of time, throughout the early part of the computational model, and especially, in the lower part of the slab. This increasing path can be seen from the first year of the simulation, till the 8,000th year.

This observation demonstrates that the relationship between stress and strain is non-linear. In fact, it appears inverse, as periods and locations where the upper layer exhibits high strain values correspond to relatively low stress levels.

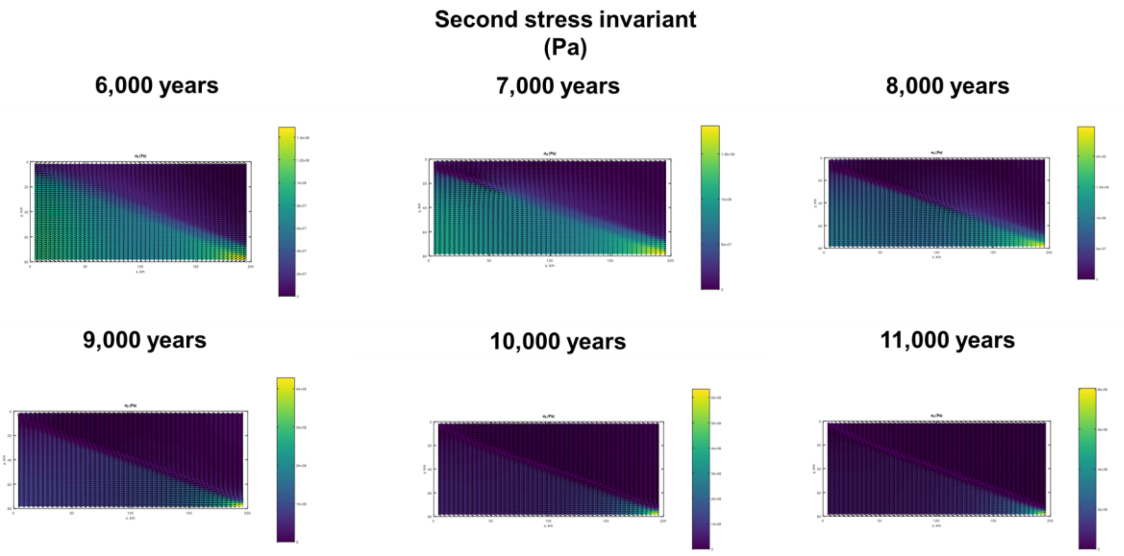

Part II

Figure 8: In part II of this figure the second stress invariant values are showcased for the computational model, when the thickness of the upper deformed layer was set at 5 km, particularly after 6,000 years from the initiation of the simulation, after 7,000 years, 8,000 years, 9,000, 10,000 and 11,000 years respectively.

Additionally, for the final 6,000 years, 9,000-15,000, of the simulation the stress values throughout almost the whole computational model are low and mostly constant with only slight deviations. The latter note makes it clear that the high strain values that can be seen inside the upper deformed layer, after the spreading of the cracks, in the 9,000th year, is most likely caused by deformation creep.

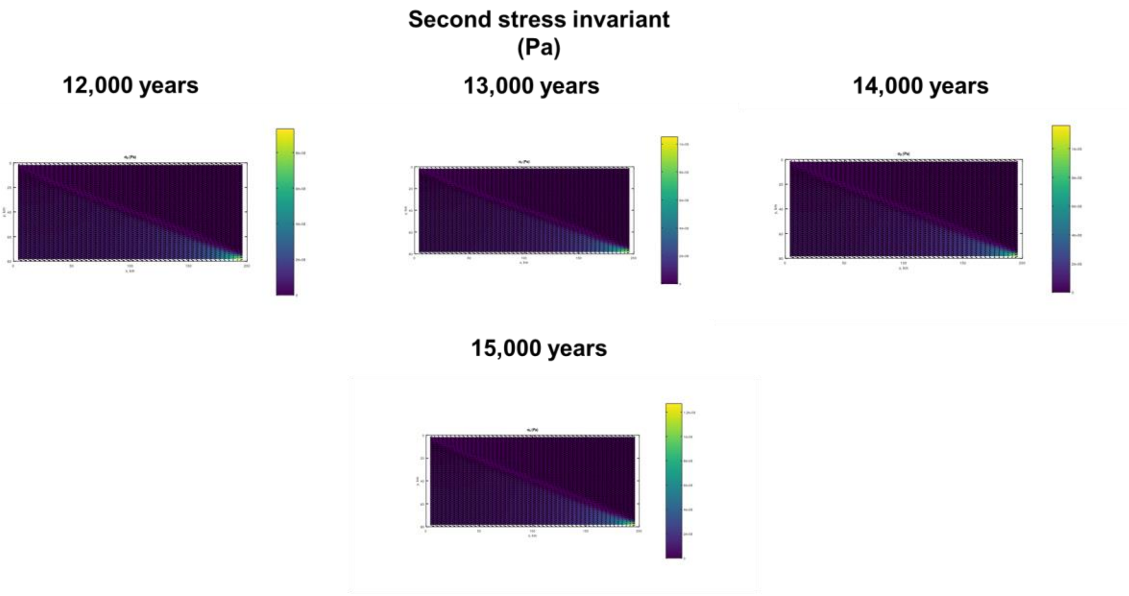

Part III

Figure 8: In part III of this figure the second stress invariant values are showcased for the computational model, when the thickness of the upper deformed layer was set at 5 km, particularly after 12,000 years from the initiation of the simulation, after 13,000 years, 14,000 and 15,000 years respectively.

Furthermore, in the three-part Figure 7, the second stress invariant values for the whole computational model are presented, when the thickness of the upper deformed part of the plate was set at 10 km. As with the 5 km model the stress values in the surface of the upper part of the plate are generally low, with the highest stress values mostly located in the lower, more stiffer parts of the plate. Moreover, it can be seen that the stress values have again a slight increasing tendency with the passage of time, throughout most of the computational model, and especially, in the lower layer of the slab. However, in contrast with the 5 km model, in this case the increasing value motive stops much earlier particularly in the 5,000th year.

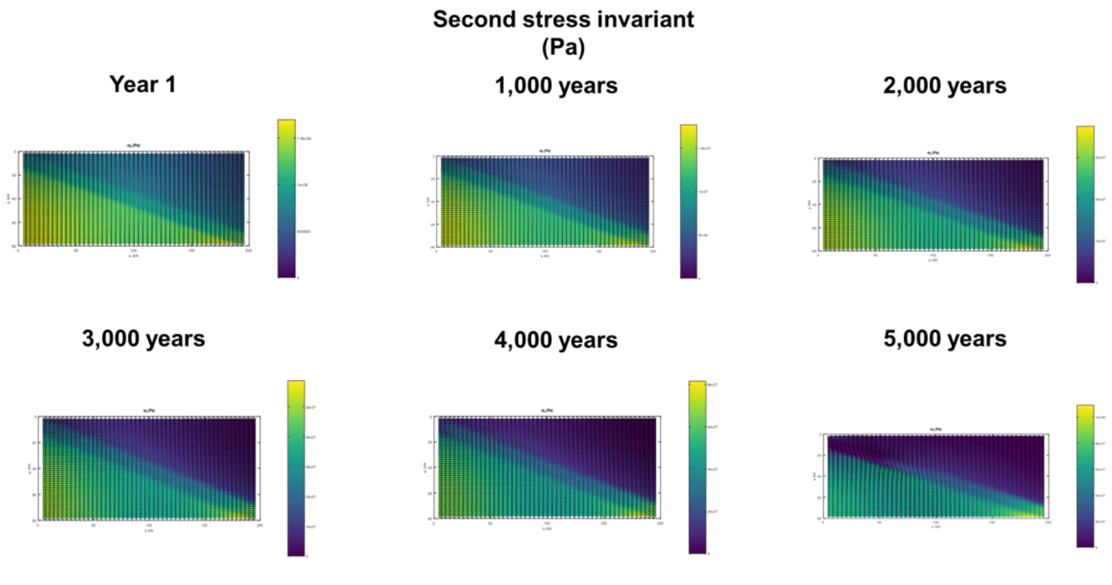

Part I

Figure 9: In part I of this figure the second stress invariant values are showcased for the computational model, when the thickness of the upper deformed layer was set at 10 km, particularly for the first year of the simulation, after 1,000 years, 2,000 years, 3,000, 4,000 and 5,000 years respectively.

From the 6,000th year till the end of the simulation, 6,000-15,000, the stress values throughout almost the whole computational model are again low and mostly constant. Overall, the primary difference between the 5 km and 10 km models is that, in the 10 km model, comparable results are observed in a significantly shorter timeframe for both strain and stress measurements. Consistent with the 5 km model, it is evident that the high strain values within the upper deformed layer, following crack propagation in the 7,000th year, are likely attributable to deformation creep.

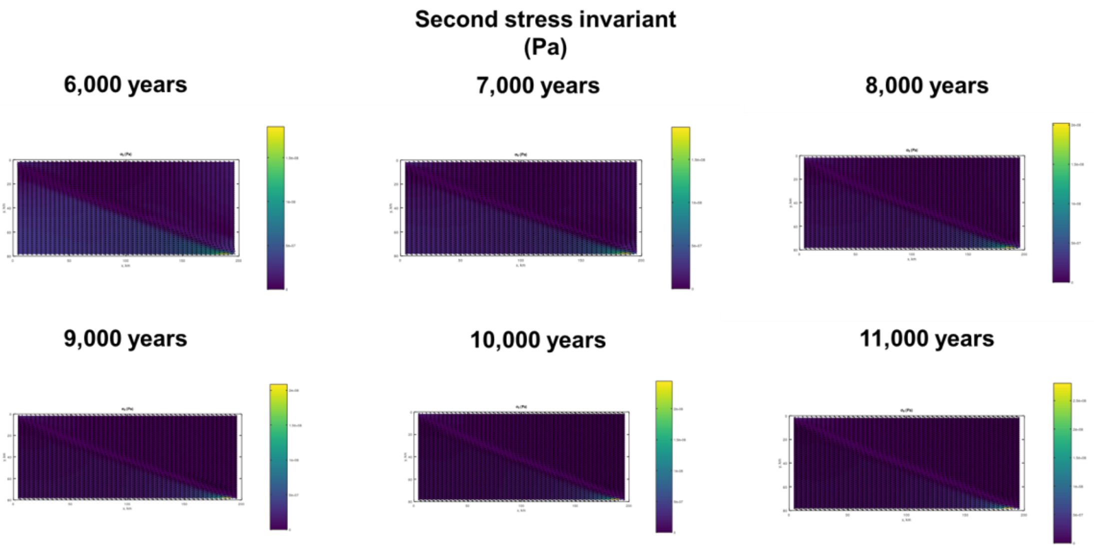

Part II

Figure 9: In part II of this figure the second stress invariant values are showcased for the computational model, when the thickness of the upper deformed layer was set at 10 km, particularly after 6,000 years from the initiation of the simulation, after 7,000 years, 8,000 years, 9,000, 10,000 and 11,000 years respectively.

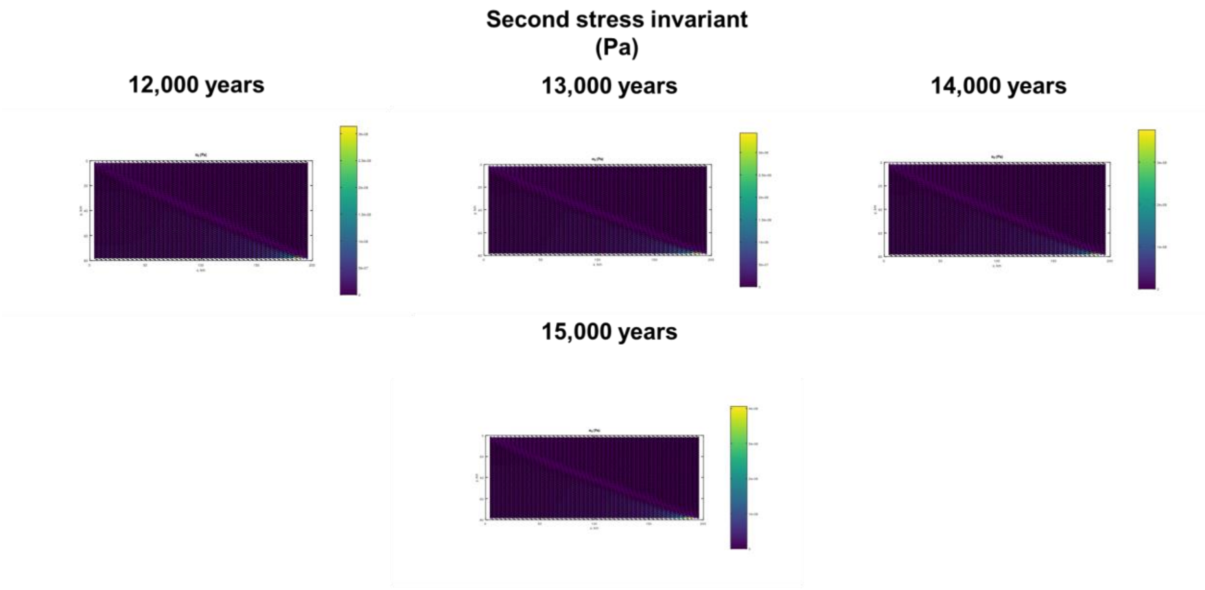

Part III

Figure 9: In part III of this figure the second strain rate invariant values are showcased for the computational model, when the thickness of the upper deformed layer was set at 10 km,

particularly after 12,000 years from the initiation of the simulation, after 13,000 years, 14,000 and 15,000 years respectively.

Additionally, Figure 10 depicts the second stress invariant values at specific time steps of the simulation, corresponding to the 49 vertical nodes situated within the upper thin layer of the plate, with a thickness set at 5 km. The analyzed time steps include the first year, the 1,000th year, and the 6,000th through 9,000th years in 1,000-year intervals, as well as the 15,000th year.

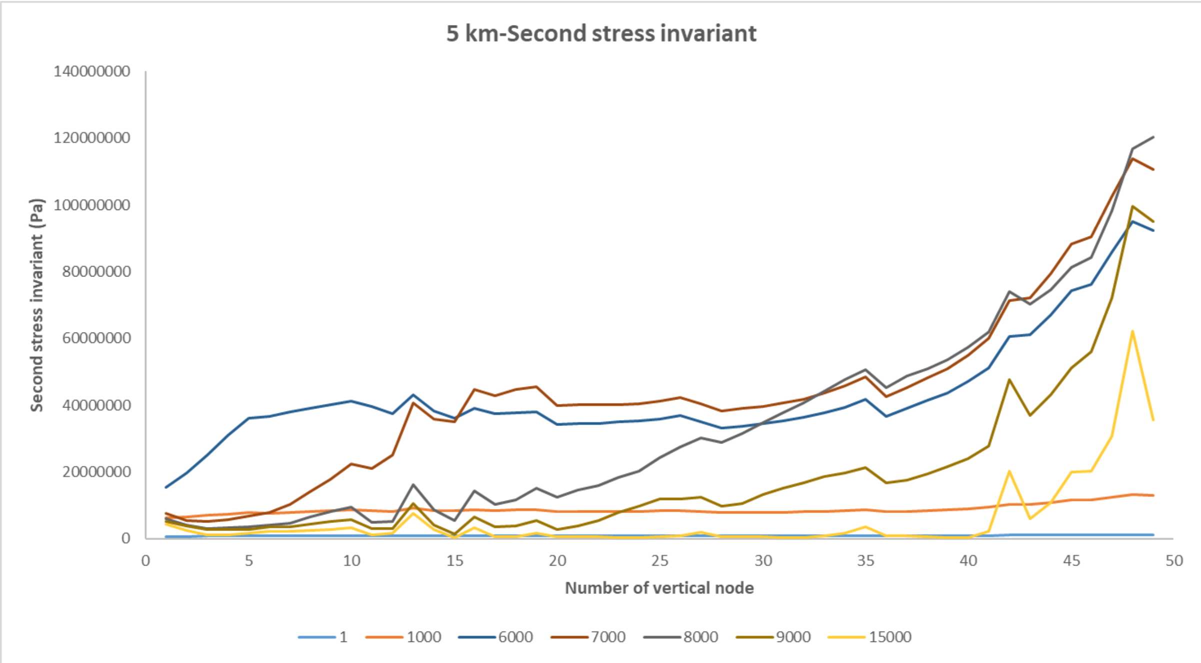

Figure 10: In this figure the second stress invariant values are presented, when the thickness of the upper layer of the plate was set at 5 km, for various important time moments of the simulation, in relation to the 49 vertical nodes that are located inside the upper deformed part of the lithospheric slab.

Generally, from the first year of the simulation until the 8,000th year, the stress values exhibit a consistent, gradual increase, particularly in the lower right section of the slab, with the values reaching their peak at the 8,000th year. In alignment with Fig. 8 (Part II), from the 9,000th year onward, the stress values are mostly stable and constant.

Similarly, Figure 11 presents the second stress invariant values, analyzed in relation to the 49 vertical nodes situated within the upper deformed layer of the plate. In this case, the slab thickness is set at 10 km. The time steps depicted in Fig. 11 correspond to the first year, the 1,000th year, the 4,000th year, and subsequent key intervals at the 5,000th, 6,000th, 9,000th, and 15,000th years after the start of the simulation.

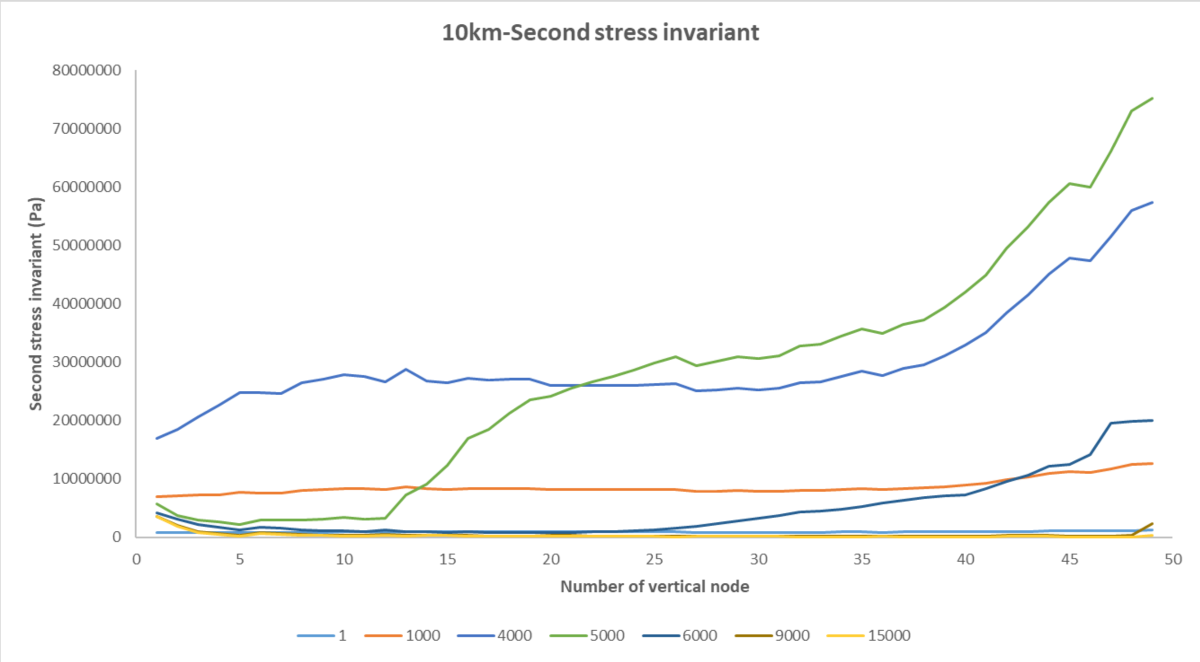

Figure 11: In this figure the second stress invariant values are presented, when the thickness of the upper layer of the plate was set at 10 km, for various important time moments of the simulation, in relation to the 49 vertical nodes that are located inside the upper deformed part of the lithospheric slab.

Similarly to the 5 km model, an initial slight increase in stress values is observed throughout the entire length of the upper layer during the first 5,000 years, coinciding with the onset of crack propagation and the potential detachment of material from the slab. From the 6,000th year onward, the stress values are mostly low and constant in nearly the entire computational model, particularly within the upper portion of the plate.

5.3. Viscosity

Overall, viscosity values exhibited only minor fluctuations over time. Figure 12, presented in three parts, shows the viscosity map of the computational model when the thickness of the plate's upper deformed layer was set to 5 km.

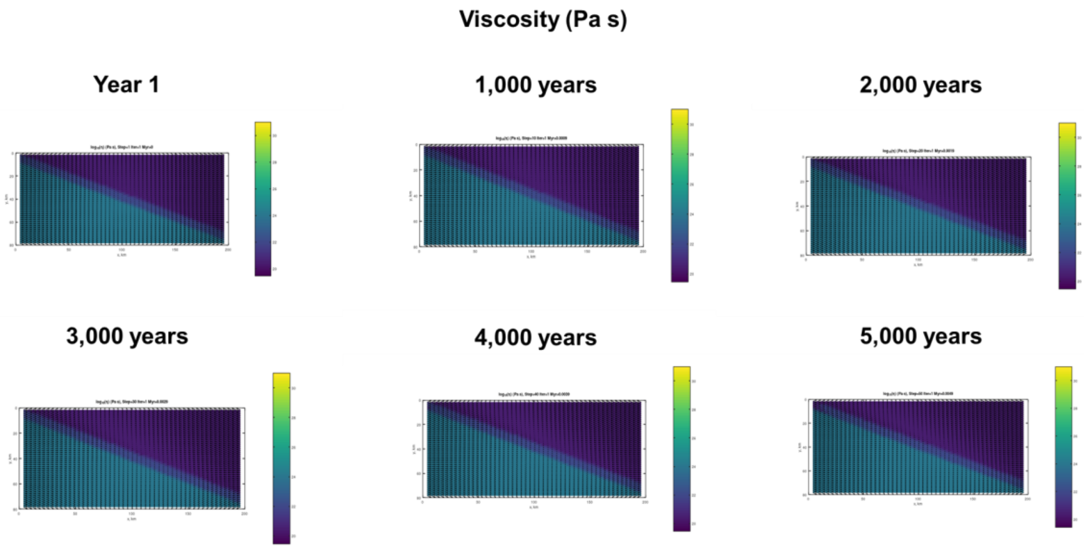

Part I

Figure 12: In part I of this figure the viscosity values are showcased for the computational model, when the thickness of the upper deformed layer was set at 5 km, particularly for the first year of the simulation, after 1,000 years, 2,000 years, 3,000, 4,000 and 5,000 years respectively.

For the first 5,000 years of the simulation the viscosity values of the mantle, the upper deformed layer and the lower stiffer layer of the plate mostly maintain their original given values constant. However, in the 6,000th year, the same year that the major cracks start to emerge in the upper left part of the plate, the viscosity values in that same area, become much lower, and closely match that of the flowing mantle, indicating that the mantle has infiltrated the upper deformed layer, through the newly formed cracks.

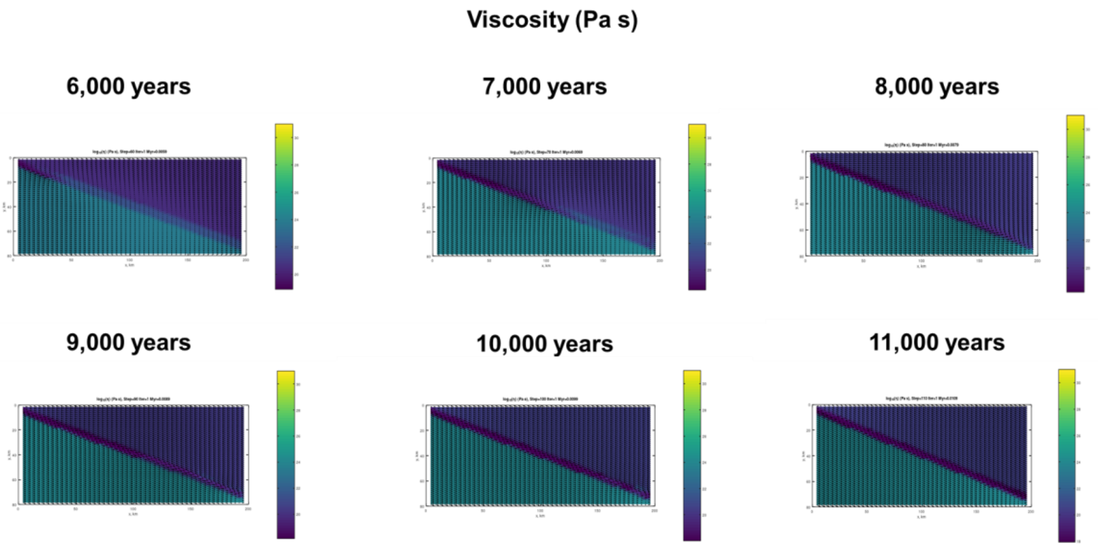

Part II

Figure 12: In part II of this figure the viscosity values are showcased for the computational model, when the thickness of the upper deformed layer was set at 5 km, particularly after 6,000 years from the initiation of the simulation, after 7,000 years, 8,000 years, 9,000, 10,000 and 11,000 years respectively.

This decrease in viscosity values spreads throughout the whole length of the upper layer, for the next 2,000 years, matching the propagation of the cracks, and perhaps the detachment of lithospheric material, and thus making the mantle enter the rest of the layer. Finally, the values of the viscosity again stabilise at the 9,000th year and remain mostly the same for the rest of the simulation.

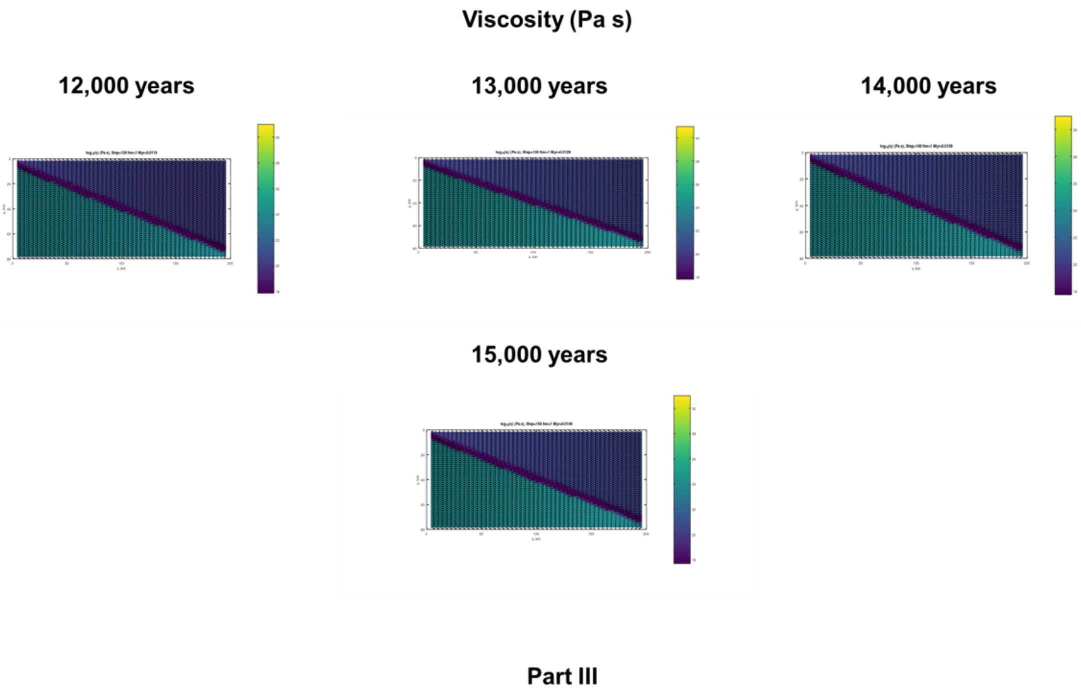

Figure 12: In part III of this figure the viscosity values are showcased for the computational model, when the thickness of the upper deformed layer was set at 5 km, particularly after 12,000 years from the initiation of the simulation, after 13,000 years, 14,000 and 15,000 years respectively.

Overall, in the three-part Figure 13, which corresponds to the viscosity values of the computational model when the thickness of the upper deformed layer was set at 10 km, the same observations can be made with the only difference being the different time moments that the same events appear. For the first 4,000 years of the simulation the original given values for the viscosity remain relatively the same. Following the 5,000th year, coinciding with the onset of crack formation and the subsequent entry of the viscous mantle into the plate's upper layer, the viscosity values in this layer begin to decrease. These reduced viscosity values, closely resembling those of the flowing mantle, spread to encompass the entire length of the heavily deformed upper layer within only 1,000 years. Consequently, from the 6,000th year until the end of the simulation, viscosity values remain consistently lower than their initial levels, as the mantle has fully infiltrated through the cracks

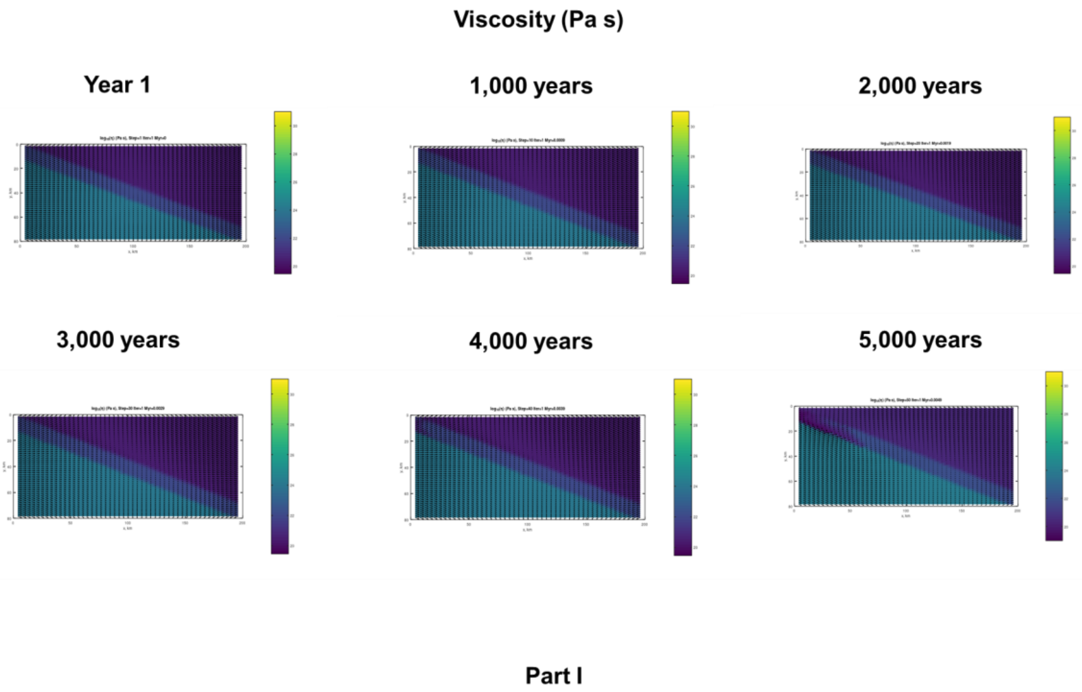

Figure 13: In part I of this figure the viscosity values are showcased for the computational model, when the thickness of the upper deformed layer was set at 10 km, particularly for the first year of the simulation, after 1,000 years, 2,000 years, 3,000, 4,000 and 5,000 years respectively.

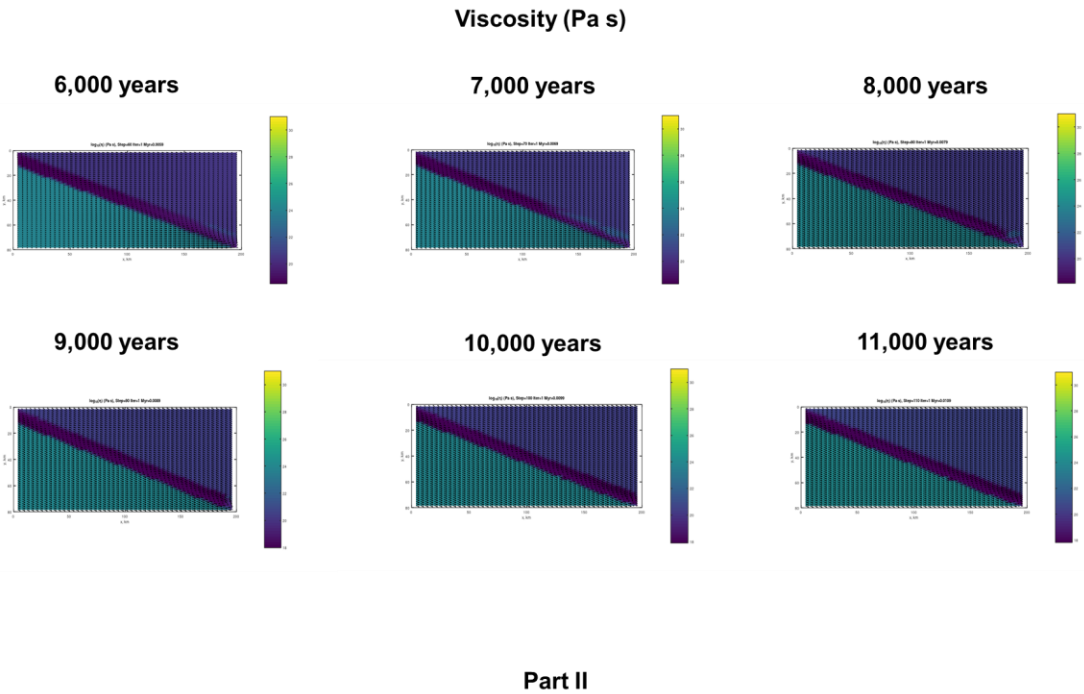

Figure 13: In part II of this figure the viscosity values are showcased for the computational model, when the thickness of the upper deformed layer was set at 10 km, particularly after

6,000 years from the initiation of the simulation, after 7,000 years, 8,000 years, 9,000, 10,000 and 11,000 years respectively.

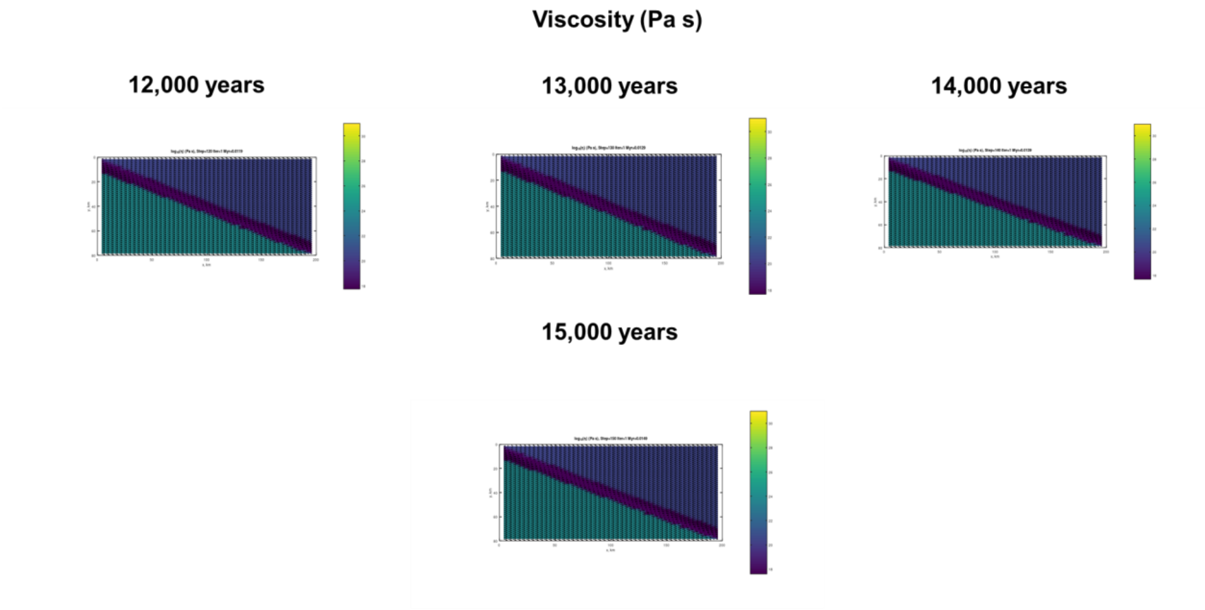

Part III

Figure 13: In part III of this figure the viscosity values are showcased for the computational model, when the thickness of the upper deformed layer was set at 10 km, particularly after 12,000 years from the initiation of the simulation, after 13,000 years, 14,000 and 15,000 years respectively.

A key observation that further supports the hypothesis of lithospheric material detachment due to extensive cracking and mantle infiltration within the plate's upper layer appears in the 7,000th year. Close examination reveals two rock segments on the upper right side of the slab's heavily deformed layer, each approximately 30 km in length, that retain their original viscosity values. This suggests that the cracks may not have yet propagated to this section of the layer, while the rest of the layer shows full crack formation and consequent mantle infiltration. By the 8,000th year, however, only a small portion, around 10 km, of the previously unaffected segments remained unchanged. This remaining segment appears semi-detached from the plate and shows an upward orientation.

In sum, this detail reinforces that the cracks initiated in both the 5 km and 10 km models create rock segments, ranging from 10 to 30 km in length, that detach from the upper plate layer, thereby allowing the mantle to fully infiltrate the surrounding highly fractured and deformed material.

6. Remarks

6.1. Stress-Strain Nonlinear Relation

In this section the nonlinear relation between arguably the two most important parameters of the computational model, the second strain invariant and the second stress invariant is further analysed. As it has been already stated there appears to be a paradoxical relation between the stress and the strain, particularly, when the stress values are high, the strain values do not follow the same pattern, but quite the opposite and the same applies for the contrary.

Overall, this important observation can be further seen in the following Figures 14 and 15, when the thickness of the upper layer of the plate was set at 5 and 10 km respectively. In the latter figures the stress and strain values are presented in relation to the simulation time, for one out of the 49 vertical nodes that are located inside the upper deformed layer of the slab.

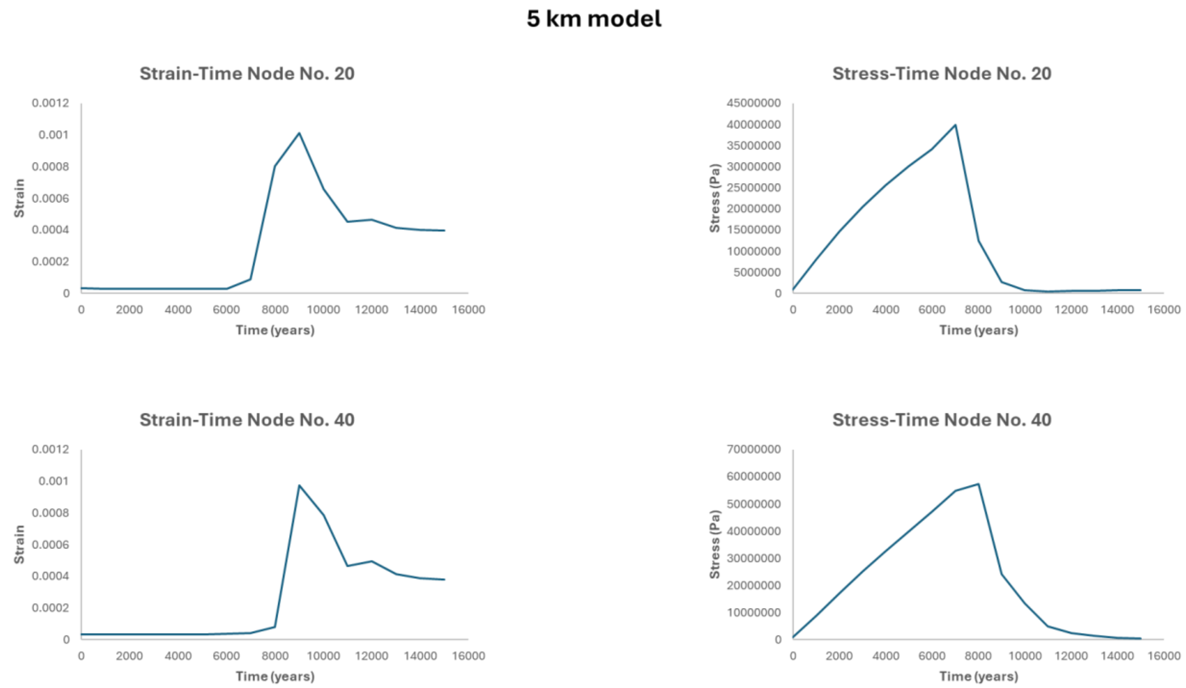

Figure 14: In this figure the stress and strain values are depicted in relation to the simulation time for the 20th and 40th node, while the thickness of the upper layer of the slab was set at 5 km.

Firstly, all of the nodes display somewhat the same results, making most of the graphs similar, and hence the 20th and 40th nodes were chosen completely randomly. As for Fig. 14, which represents the 5 km model, it can be clearly seen that for the first 6,000 years of the simulation the stress values are constantly increasing almost linearly, while at the same time the strain values inside the upper layer of the plate are almost zero. As it has been previously stated this can be easily explained because the stress that is exerted inside the layer may not be sufficient to cause any major, or noteworthy strain, since the stress values have a range of

5-40 MPa, which are relatively really low values when taking into account the geodynamic process that is taking place.

However, after the 7,000th year for the 20th node, it appears that the upper layer developed enough stress, to cause cracks, and to generally generate deformation, hence the increasing strain values. The cracks needed around 1,000 years to propagate to the 40th node, thus explaining that the values of strain increased there almost 1,000 years later. Generally, with the initiation of the cracks and commencement of the increase in strain values, the stress values suddenly decrease fast, further explaining and justifying that major cracks occurred in the length of the upper layer of the plate, because with the development of cracks comes stress release.

Despite the sudden decrease in the stress values, and especially, in the node numbers 10-40, the strain values maintain a constant high value. This can be only attributed to the development of diffusion creep (Gerya et al., 2002; Gerya, 2010). In general, creep deformation is time-dependent and occurs under constant stresses (Gariboldi and Spigarelli, 2019), just like in the present case. Creep deformation is a very common phenomenon in subducting plates that has been observed and studied by many previous researchers (Stöckhert, 2002; Wassmann and Stöckhert, 2013; Agard et al., 2020).

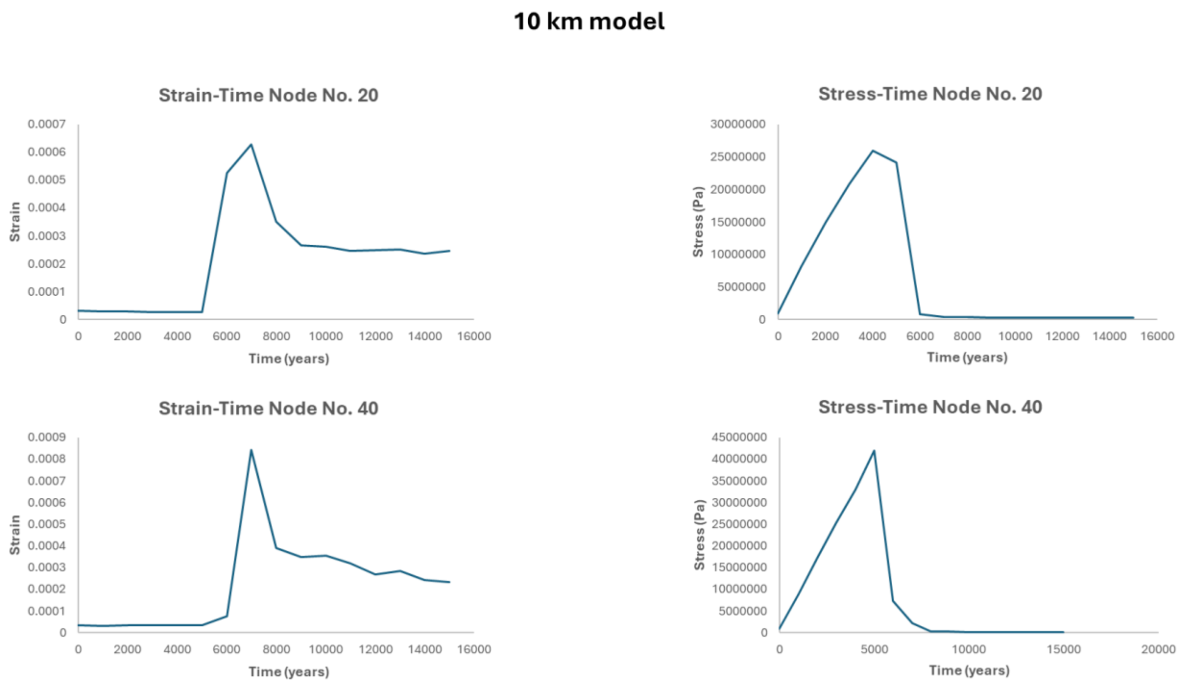

Figure 15: In this figure the stress and strain values are depicted in relation to the simulation time for the 20th and 40th node, while the thickness of the upper layer of the slab was set at 10 km.

Similarly, in Figure 15, which corresponds to the 10 km model, observations align with those of the 5 km model, with the primary distinction being that these events occur earlier. Specifically, stress decreases while strain increases, beginning at the 20th node around the 4,000th year. By approximately the 7,000th year, stress reaches a low, stable value, and creep deformation initiates.

6.2. Effect of the Thickness of the Upper Deformed Layer of the Subducting Plate

Overall, another key insight drawn from the simulation results suggest that the thickness of the upper deformed layer of the subducting plate only influences the timing of which the same events will occur. Specifically, by increasing the thickness of the layer, its structural strength is reduced. In the 10 km model, cracks, potential material detachment, and viscous mantle infiltration occur within 5,000 years and subsequently propagate along the entire layer. In contrast, in the 5 km model, this sequence begins 1,000 years later, in the 6,000th year.

7. Comparison with Observations from the Hellenides

The final step in supporting the aforementioned assumptions involves examining whether metamorphic rocks of this nature are present in the broader Hellenides region and attempting to identify the depths from which they originated. Furthermore, it is crucial to note that after detachment from the upper portion of the subducting plate, it is highly probable that such rocks would require millions of years to re-emerge at the Earth's surface. Initially, these rocks are expected to remain within the viscous flowing mantle, where the high-pressure, low-temperature conditions facilitate their metamorphism from granite to quartzites and phyllites occurs. At the typical detachment depth of approximately 30 km, mantle temperatures are around 520 K (approximately 250°C). The lithostatic pressure at this depth can be estimated using the following equation (Turcotte and Schubert, 1982):

$$P_L = \rho g y \ (20),$$

where, P_L: is the lithostatic pressure, ρ: is the density of the detached segment and y: is the depth from the surface. Consequently, the pressure exerted on the segment is approximately 824 MPa. These pressure-temperature (P-T) conditions are classified as high-pressure and low-temperature (HP/LT). Thus, it is essential to investigate whether any HP/LT exhumed metamorphic rocks exist within the Hellenides and to estimate the time required for their exhumation. However, it is critical to establish that, if such exhumed rocks are identified, they originated from the same detachment depth as those observed in the simulation. This would confirm that shallow-depth rocks, detached from the upper part of the subducting lithospheric plate in under 10,000 years, can indeed undergo exhumation.

A comprehensive study by Thomson et al. (1998) highlights the presence of HP/LT exhumed metamorphic rocks within the Hellenides, particularly in Crete. The study further indicates that these HP/LT rocks predominantly consist of quartz and phyllite, two common minerals found in gneiss. Moreover, it is reported that these rocks were originally detached from the lower subducting lithospheric plate at depths of approximately 30–35 km, where they also underwent metamorphism shortly after detachment (Thomson et al., 1998). Finally, the P-T conditions at which the metamorphism occurred match that of the computational setting, particularly, the maximum temperature was found to be around $300 \pm 50^{o}\mathrm{C}$ and the pressure $800 \pm 300\ MPa$ (Thomson et al., 1998). It should be noted that various others researchers have investigated the HP/LT exhumed metamorphic rocks that appear in Crete

(Fassoulas et al., 1994; Chatzaras et al., 2006; Ring et al., 2010), with the most complete and systematic study being that of Thomson et al. (1998).

8. Discussion and Conclusions

In this study a two-dimensional thermomechanical visco-elasto-plastic code, originally created by Gerya (2010), was heavily modified in order to simulate the subducting plate of the Mediterranean ridge. The aim of the study was firstly to investigate whether at the shallow depths of the lithosphere, particularly close to 30 km, if the upper deformed part of the downgoing plate endures such increased strain values that the detachment of segments occurs. The simulation results clearly showcased that major cracks begin to propagate (see Fig. 4 part II for the 5 km model and Fig. 5 part I for the 10 km model) for both model sizes, and in general after a very short geological time. For the 5 km model (see the three-part Fig. 4) the cracks initiated after only 6,000 years, as for the 10 km model (see the three-part Fig. 5) the cracks initiated 1,000 years earlier, after only 5,000 years. After the initiation of the cracks, the latter slowly propagated towards the lower parts of the upper section of the plate (see Fig. 4 part II, III and Fig. 5 part II), until they had covered the whole length of the layer.

Additionally, it was observed that the viscosity values of the ‘’broken’’ upper layer showcased a significant drop (see Fig. 12 part II for the 5 km model and Fig. 13 part I for the 10 km model), and the values closely aligned with those of the flowing mantle, thus indicating that the latter infiltrated the newly formed cracks and started flowing through the cracks of the layer. Furthermore, another important assumption that was derived from the simulation results was the non-linear relation between the stress and strain values on the surface of the plate and inside the upper deformed layer of the plate (see Fig. 14 for the 5 km model and Fig. 15 for the 10 km model). At the initial stages of the simulation, this paradoxical relation was attributed to the very low stress values, around 5-40 MPa, that can be deemed insufficient to cause any major strain deformation on the subducting slab. As for the later stages of the computational model, this non-linear relation can be easily attributed due to the development of diffusion creep inside the heavily broken and deformed upper part of the plate, a phenomenon that has been studied and observed by various researchers over the past decades (Gerya et al., 2002; Stöckhert, 2002; Gerya, 2010; Wassmann and Stöckhert, 2013; Agard et al., 2020).

Moreover, an additional significant observation from the computational model, which supports the authors hypothesis, that during the initiation and the propagation of the cracks, respectively, medium to small size segments from the upper part of the layer were completely detached, was seen in the 10 km model after 7,000 years that the simulation had started (see Fig. 13 part II). Particularly, it was clearly seen that small rock segments, having a length of around 10-30 km, had kept their original given viscosity value and they were semi-detached from the plate, while at the same time having an upwards motion. After all the aforementioned assumptions, the natural question that arose was if these detached segments of rock ever made it back to the surface, thus getting exhumed.

Another very common and more simpler exhumation mechanism that has been suggested is that the detached rock is driven upwards, and consequently exhumed, due to the density difference between the flowing mantle and the density of the segment (Liou et al., 2004; Warren et al., 2008a, 2008b; Beaumont et al., 2009; Warren, 2013), thus producing a upwards buoyancy driven force, capable of exhuming the detached rock. The latter model can be easily considered suitable for the current setting since all the necessary prerequisites were present in the computational model. Finally, having proven that segments are detached from the downgoing plate, at a relatively shallow depth of around 30 km, and knowing that the Mediterranean ridge setting favours one of the many proposed exhumation mechanisms, the only important question remaining is whether rocks of that types have ever been observed in the surface of the Hellenides.

The detached rocks from the subducting plate were subjected to high pressure and relatively low temperature conditions for an extended period of time, thus making them HP/LT metamorphic rocks. Overall, such HP/LT exhumed metamorphic rock have been widely studied and observed in the Greek island of Crete (Fassoulas et al., 1994; Thomson et al., 1998; Chatzaras et al., 2006; Ring et al., 2010). Particularly, the in-depth study by Thomson et al. (1998) clearly indicated that these HP/LT exhumed metamorphic rocks had been detached from the downgoing plate from the shallow depths of around 30-35 km. In addition, by using thermochronology the researchers identified that the detachment of the segments occurred around 24 to 19 Ma ago.

To sum up, in this study a combination of computational, theoretical techniques and macroscopic observations were utilised to fully investigate whether shallow depth rocks are detached from the subducting plate, in the Mediterranean ridge, and consequently, if they ever reach the surface of the Earth again, in the broader area of the Hellenides. The general results and assumptions of the study indicated and proved that the latter process does occur in the subduction setting of the Mediterranean ridge. Overall, due to the limited available literature on the subject of modelling and mechanisms of shallow depth detachment of material from a subducting plate, the current simulation results and general efforts serve as a stepping stone to a process that requires more analysis and investigations from researchers in the future. An important future step, and consequent idea for research, towards the better understanding of the mechanisms behind the latter process is to fully incorporate the subducting rate parameter of the plate in future computational models, in order to make the model even more realistic, a parameter that was neglected in the present study due to the short geological time of the simulation.

Appendix

Additional material that further explains the structure and mechanisms of the utilised code, as well as access to the modified version of the code used by the authors during the simulation will be provided upon request to the corresponding author.

Acknowledgments

The authors would like to thank Maria-Sotiria Frousiou and Stefanos Petrakopoulos for designing Figure 1 and 2 respectively.

References

Agard, P., Prigent, C., Soret, M., Dubacq, B., Guillot, S., Deldicque, D., 2020. Slabitization: Mechanisms controlling subduction development and viscous coupling. Earth-Science Reviews (2020), Vol. 208, 103259. doi: https://doi.org/10.1016/j.earscirev.2020.103259.

Albers, M., 2000. A local mesh refinement multigrid method for 3D convection problems with strongly variable viscosity. J. Comput. Phys. (2000), Vol. 160, pp. 126–150.

Beaumont, C., Jamieson, R., A., Butler, J., P., Warren, C., J., 2009. Crustal structure: A key constraint on the mechanism of ultra-high-pressure rock exhumation. Earth and Planetary Science Letters (2009), Vol. 287, pp. 116–129. doi: 10.1016/j.epsl.2009.08.001.

Capitanio, F., A., Morra, G., Goes, S., 2007. Dynamic models of downgoing plate-buoyancy driven subduction: Subduction motions and energy dissipation. Earth and Planetary Science Letters (2007), Vol. 262, pp. 284–297. doi: 10.1016/j.epsl.2007.07.039.

Chapple, W., M., Tullis, T., E., 1977. Evaluation of forces that drive plates. J. Geophys. Res., Vol. 82, pp. 1967–1984.

Chatzaras, V., Xypolias, P., Doutsos, T., 2006. Exhumation of high-pressure rocks under continuous compression: a working hypothesis for the southern Hellenides (central Crete, Greece). Geological Magazine, Vol. 143, Issue 6, pp. 859-876, November 2006. doi: https://doi.org/10.1017/S0016756806002585.

Chemenda, A., I., Mattauer, M., Bokun, A., N., 1996. Continental subduction and a mechanism for exhumation of high-pressure metamorphic rocks: new modelling and field data from Oman. Earth and Planetary Science Letters (1996), Vol. 143, pp. 173-182.

Christensen, U., 1982. Phase boundaries in finite amplitude mantle convection. Geophysical Journal of the Royal Astronomical Society, Vol. 68, pp. 487–97.

Cloos, M., 1982. Flow melanges; numerical modeling and geologic constraints on their origin in the Franciscan subduction complex, California. Geol. Soc. Am. Bull., Vol. 93, pp. 330–344.

Cloos, M., Shreve, R., L., 1988a. Subduction-channel model of prism accretion, melange formation, sediment subduction, and subduction erosion at convergent plate margins; Part I, Background and description. Pure Appl. Geophys., Vol. 128, pp. 455–500.

Cloos, M., Shreve, R., L., 1988b. Subduction-channel model of prism accretion, melange formation, sediment subduction, and subduction erosion at convergent plate margins; Part II, Implications and discussion. Pure Appl. Geophys., Vol. 128, pp. 501–545.

Davies, G., F., 1988. Role of the lithosphere in mantle convection. J. Geophys. Res., Vol. 93, pp. 10451–10466.

England, P., C., Holland, T., J., B., 1979. Archimedes and the Tauern eclogites: the role of buoyancy in the preservation of exotic tectonic blocks. Earth Planet. Sci. Lett., Vol. 44, pp. 287–294.

Fassoulas, C., Kilias, A., Mountrakis, D., 1994. Postnappe stacking extension and exhumation of high-pressure/low-temperature rocks in the island of Crete, Greece. Tectonics, Vol. 13, No. 1, pp. 127-138, February 1994.

Forsyth, D., Uyeda, S., 1975. On the relative importance of driving forces of plate motion. Geophys. J. R. Astron. Soc., Vol. 43, pp. 163–200.

Gariboldi, E., Spigarelli, S., 2019. Creep and High-Temperature Deformation of Metals and Alloys. Metals 2019, 9(10), 1087; doi: https://doi.org/10.3390/met9101087.

Gerya, T., V., 2010. Introduction to Numerical Geodynamic Modelling. Cambridge University Press, First Edition. doi: https://doi.org/10.1017/9781316534243.

Gerya, T., V., Stöckhert, B., Perchuk, A., L., 2002. Exhumation of high-pressure metamorphic rocks in a subduction channel: A numerical solution. Tectonics (2002), Vol. 21, No. 6, 1056, doi: 10.1029/2002TC001406.

Gerya, T., V., Yuen, D., A., 2003a. Rayleigh-Taylor instabilities from hydration and melting propel 'cold plumes' at subduction zones. Earth and Planetary Science Letters (2003), Vol. 212, pp. 47-62. doi: 10.1016/S0012-821X(03)00265-6.

Gerya, T., V., Yuen, D., A., 2003b. Characteristics-based marker-in-cell method with conservative finite-differences schemes for modeling geological flows with strongly variable transport properties. Physics of the Earth and Planetary Interiors (2003), Vol. 140, pp. 293–318. doi: 10.1016/j.pepi.2003.09.006.

Ghosh, D., Maiti, G., Mandal, N., Baruah, A., 2020. Cold Plumes Initiated by Rayleigh-Taylor Instabilities in Subduction Zones, and Their Characteristic Volcanic Distributions: The Role of Slab Dip. Journal of Geophysical Research: Solid Earth, Vol. 125, e2020JB01981. doi: https://doi.org/10.1029/2020JB019814.

Goes, S., Capitanio, F., A., Morra, G., Seton, M., Giardini, D., 2011. Signatures of downgoing plate-buoyancy driven subduction in Cenozoic plate motions. Physics of the Earth and Planetary Interiors (2011), Vol. 184, pp. 1–13. doi: 10.1016/j.pepi.2010.10.007.

Gustafsson, B., 2008. High Order Finite-Difference Methods for Time-dependent PDE. Springer-Verlag (2008).

Kaus, B., J., P., Becker, T., W., 2007. Effects of elasticity on the Rayleigh–Taylor instability: implications for large-scale geodynamics. Geophys. J. Int. (2007), Vol. 168, pp. 843–862. doi: 10.1111/j.1365-246X.2006.03201.x.

Li, Z., H., 2014. A review on the numerical geodynamic modeling of continental subduction, collision and exhumation. Science China, Earth Sciences, Vol. 57, pp. 47-69. doi: 10.1007/s11430-013-4696-0.

Li, Z., H., Xu, Z., Q., Gerya, T., V., Ahmand, D., I., 2012. Numerical geodynamic modeling of continental convergent margins. Earth Sciences, Chapter 13.

Liou, J., G., Tsujimori, T., Zhang, R., Y., Katayama, I., and Maruyama, S., 2004. Global UHP metamorphism and continental subduction/collision, the Himalayan model. Int. Geol. Rev., Vol. 46, pp. 1-27, 2004.

Lynch, D., R., 2005. Numerical Partial Differential Equations for Environmental Scientists and Engineers: A Practical First Course. Springer-Verlag (2005).

Makris, J., 2010. Geophysical studies and tectonism of the Hellenides, Bull. Geol. Soc. Greece, XLIII (1), pp. 32–45.

Makris, J., Papoulia, J., Yegorova, T., 2013. A 3-D density model of Greece constrained by gravity and seismic data. Geophys. J. Int. (2013), Vol. 194, pp. 1–17. doi: 10.1093/gji/ggt059.

Mancktelow, N., S., 1995. Nonlithostatic pressure during sediment subduction and the development and exhumation of high-pressure metamorphic rocks. J. Geophys. Res., Vol. 100, pp. 571–583.

Moresi, L., N., Solomatov, V., S., 1995. Numerical investigation of 2D convection with extremely large viscosity variations. Phys. Fluids (1995), Vol. 7, pp. 2154–2162.

Neil, E., A., Houseman, G., A., 1999. Rayleigh-Taylor instability of the upper mantle and its role in intraplate orogeny. Geophys. J. Int. (1999), Vol. 138, pp. 89-107.

Platt, J., P., 1993. Exhumation of high-pressure rocks: a review of concepts and processes. Terra Nova, Vol. 5, Issue 2, pp. 119-133. doi: https://doi.org/10.1111/j.1365-3121.1993.tb00237.x.

Pozrikidis, C., 2001. Fluid Dynamics: Theory, Computation and Numerical Simulation. Pp. 675, Kluwer Acad., Boston, Mass.

Raimbourg, H., Jolivet, L., Leroy, Y., 2007. Consequences of progressive eclogitization on crustal exhumation, a mechanical study. Geophys. J. Int. (2007), Vol. 168, pp. 379–401. doi: 10.1111/j.1365-246X.2006.03130.x.

Ring, U., Glondy, J., Will, T., Thomson, S., 2010. The Hellenic Subduction System: High-Pressure Metamorphism, Exhumation, Normal Faulting, and Large-Scale Extension. Annual Review of Earth and Planetary Sciences (2010), Vol. 38, pp. 45-76. doi: https://doi.org/10.1146/annurev.earth.050708.170910.

Royden, L., H., Papanikolaou, D., J., 2011. Slab segmentation and late Cenozoic disruption of the Hellenic arc. Geochem. Geophys. Geosys. (G3), Vol. 12, No. 3, Q03010. doi: 10.1029/2010GC003280.

Rubatto, D., Hermann, J., 2001. Exhumation as fast as subduction?. Geology, Vol. 29, pp. 3–6. doi: 10.1130/0091 7613(2001)029<0003:EAFAS>2.0.CO;2, 2001.

Schmeling, H., 1987. On the relation between initial conditions and late stages of Rayleigh-Taylor instabilities. Tectonophysics, Vol. 133, pp. 65–80.

Stöckhert, B., 2002. Stress and deformation in subduction zones: insight from the record of exhumed metamorphic rocks. Geological Society, London, Special Publications, Vol. 200, pp. 255-274. doi: https://doi.org/10.1144/GSL.SP.2001.200.01.15.

Thomson, S., N., Stöckhert, B., Brix, M., R., 1998. Miocene high-pressure metamorphic rocks of Crete, Greece: rapid exhumation by buoyant escape. Geological Society, London, Special Publications, Vol. 154 (1), pp. 87-107. doi: 10.1144/gsl.sp.1999.154.01.04.

Trompert, R., A., Hansen, U., 1996. The application of a finite-volume multigrid method to three-dimensional flow problems in a highly viscous fluid with variable viscosity. Geophys. Astrophys. Fluid Dyn. (1996), Vol. 83, pp. 261–291.

Turcotte, D., L., Schubert, G., 1982. Geodynamics. Cambridge University Press, Second Edition. doi: https://doi.org/10.1017/CBO9780511807442.

Vlaar, N., J., Wortel, M., J., R., 1976. Lithospheric aging, instability and subduction. Tectonophysics, Vol. 32, pp. 331–351.

Warren, C., J., Beaumont, C., Jamieson, R., A., 2008a. Formation and exhumation of ultra-high pressure rocks during continental collision: role of detachment in the subduction channel. Geochem. Geophys. Geosys. (G3), Vol. 9, No. 4. doi: 10.1029/2007GC001839.

Warren, C., J., Beaumont, C., Jamieson, R., A., 2008b. Deep subduction and rapid exhumation: Role of crustal strength and strain weakening in continental subduction and ultrahigh-pressure rock exhumation. Tectonics (2008), Vol. 27, TC6002. doi: 10.1029/2008TC002292.

Warren, C., J., 2013. Exhumation of (ultra-)high-pressure terranes: concepts and mechanisms. Solid Earth, Vol. 4, pp. 75-92, 2013. doi: 10.5194/se-4-75-2013.

Wassmann, S., Stöckhert, B., 2013. Rheology of the plate interface - Dissolution precipitation creep in high pressure metamorphic rocks. Tectonophysics (2013), Vol. 608, pp. 1-29. doi: http://dx.doi.org/10.1016/j.tecto.2013.09.030.

Weinberg, R., B., Schmeling, H., 1992. Polydiapirs: multiwavelength gravity structures. Journal of Structural Geology, Vol. 14, pp. 425–36.

Woidt, W., D., 1978. Finite-element calculations applied to salt dome analysis. Tectonophysics, Vol. 50 (2–3), pp. 369–86.

Zhong, S., J., Yuen, D., A., Moresi, L., N., 2007. Numerical methods in mantle convection. In Bercovici, D. (ed.) Treatise in Geophysics, Vol. 7, (editor-in-chief: Gerard Schubert), Elsevier, pp. 227–52.